A&A, 713, A319 (2026)
https://doi.org/10.1051/0004-6361/202660447
© The Authors 2026

Astronomy & Astrophysics

H I 21-cm absorption in low- and high-excitation radio-loud active galactic nuclei at $z < 0.5$ from the MeerKAT Absorption Line Survey

P. P. Deka[1,2,3,⋆], N. Gupta[1], J-.K. Krogager[4,5], S. A. Balashev[6], H.-W. Chen[7], F. Combes[8], H.-R. Klöckner[9], and P. Noterdaeme[10]

[1] Inter-University Centre for Astronomy and Astrophysics, Post Bag 4, Ganeshkhind, Pune 411 007, India
[2] Department of Astronomy, University of Cape Town, Private Bag X3, Rondebosch 7701, South Africa
[3] SARAO, 2 Fir Street, Black River Park, Observatory 7925, South Africa
[4] Université Lyon1, ENS de Lyon, CNRS, Centre de Recherche Astrophysique de Lyon UMR5574, 69230 Saint-Genis-Laval, France
[5] French-Chilean Laboratory for Astronomy, IRL 3386, CNRS and Universidad de Chile, Santiago, Chile
[6] Ioffe Institute, 26 Politeknicheskaya st., St. Petersburg, 194021, Russia
[7] Department of Astronomy and Astrophysics, The University of Chicago, 5640 S. Ellis Avenue, Chicago, IL 60637, USA
[8] Observatoire de Paris, Collège de France, PSL University, Sorbonne University, CNRS, LUX, Paris, France
[9] Max-Planck-Institut für Radioastronomie, Auf dem Hügel 69, 53121 Bonn, Germany
[10] Institut d'Astrophysique de Paris, UMR 7095, CNRS-SU, 98bis bd Arago, 75014 Paris, France

Received 15 April 2026 / Accepted 21 July 2026

ABSTRACT

We present results from a search of cold neutral gas associated with radio-loud active galactic nuclei (AGNs) at $z < 0.5$ – corresponding to a lookback time of ∼36% of the age of the Universe – using H I 21-cm absorption line measurements from the MeerKAT Absorption Line Survey (MALS). Crossmatching the MALS 1006 MHz catalog with the SDSS DR18 spectroscopic catalog yields 1908 radio sources at $z < 0.5$. Of these, 613 are classified as AGNs using Baldwin-Phillips-Terlevich (BPT) diagnostics and radio luminosity criteria. We further classify 426 AGNs into 327 low-excitation radio galaxies (LERGs) and 99 high-excitation radio galaxies (HERGs) using a framework combining multiple optical emission-line diagnostics. We find a significant ($>3\sigma$) difference in k-corrected $g - r$ color, consistent with LERGs residing in older galaxies with quenched star formation. We search a radio-bright subsample of 79 LERGs and 20 HERGs ($S_{1.4\ \mathrm{GHz}} > 4$ mJy) for associated H I 21-cm absorption using MALS L-band spectra. This subsample spans nearly six decades in radio luminosity (log $L_{1.4\ \mathrm{GHz}}$ (W Hz^{-1}) ∼21.1–27.0), reaching luminosities an order of magnitude fainter than previous targeted H I surveys. We report five new detections (four LERGs, one HERG) at $0.29 < z < 0.47$, yielding an overall detection rate of 3^{+3}_{-2}% at a 3σ integrated optical depth sensitivity threshold of 10.0 km s^{-1}. This rate is consistent with sensitivity-matched low-z (<0.2) samples, suggesting no significant redshift evolution out to $z \sim 0.5$ or dependence on radio luminosity. We quantify absorption-line properties using velocity offset, asymmetry, and width. In three systems, absorption is entirely redshifted relative to the systemic velocity; in the remaining two, it is predominantly blueshifted, indicating complex gas kinematics. H I profiles associated with LERGs show a wide range of asymmetries and velocity offsets exceeding 350 km s^{-1}, indicative of disturbed cold-gas kinematics likely driven by lobe expansion or jet activity.

Key words. evolution – ISM: kinematics and dynamics – galaxies: active – galaxies: evolution – quasars: absorption lines

1. Introduction

The population of radio-loud active galactic nuclei (AGNs) exhibits two distinct classes based on the nature of accretion and the accreting gas (see Heckman & Best 2014, for a review): (i) low-excitation radio galaxies (LERGs), where the central supermassive black hole (SMBH) is believed to be fueled by accretion of hot halo gas at rates <1% of the Eddington rate through a geometrically thick but optically thin accretion disk; and (ii) high-excitation radio galaxies (HERGs), where the SMBH is known to accrete cold gas at higher rates, >1% of the Eddington rate, through a geometrically thin but optically thick accretion disk. Observationally, they are distinguished based on the strength of high-excitation emission lines (e.g., [O III]) in their optical spectra relative to low-excitation lines, such as [N II], [S II], and [O I], as the radiatively efficient central AGNs in HERGs lead to stronger emission lines of higher ionization compared to LERGs. The corresponding host galaxies also exhibit fundamental differences, with LERGs primarily hosted by galaxies having higher stellar and black hole masses and older stellar populations compared to HERGs. In the nearby Universe ($z < 0.3$), LERGs display both Fanaroff and Riley I and II (FRI/II; Fanaroff & Riley 1974) morphologies, while HERGs are predominantly FRII. Additionally, the luminosity function of LERGs indicates little to no redshift evolution, or even negative evolution, whereas HERGs exhibit strong and positive evolution in their comoving space density across all radio powers (Buttiglione et al. 2010; Best & Heckman 2012; Best et al. 2014).

The two classes also display fundamentally distinct feedback mechanisms (see Best & Heckman 2012; Pracy et al. 2016; Singha et al. 2021, and the references therein). In HERGs,

⋆ Corresponding author: partha.deka@uct.ac.za

Open Access article, published by EDP Sciences, under the terms of the Creative Commons Attribution License (https://creativecommons.org/licenses/by/4.0), which permits unrestricted use, distribution, and reproduction in any medium, provided the original work is properly cited.
This article is published in open access under the Subscribe to Open model. Subscribe to A&A to support open access publication.

radiatively efficient accretion onto the SMBH produces powerful radiative or quasar-mode feedback, often manifesting as high-velocity winds and broad ionized outflows driven by energy or radiation pressure (Mullaney et al. 2013; Harrison et al. 2014). These can couple strongly to the host galaxy's ISM, heating, ionizing, and/or relocating large amounts of gas, thereby regulating star formation on galactic scales. In contrast, LERGs accrete via radiatively inefficient flows, leading to feedback dominated by kinetic or radio-mode processes. This typically involves collimated relativistic jets that interact with the surrounding medium, inflating cavities in the hot halo gas, suppressing cooling flows in clusters and groups, and driving multiphase gas outflows (Best & Heckman 2012; Gitti et al. 2012; Chandola et al. 2020; Morganti 2017). Such jet–ISM interactions can introduce strong kinematic disturbances into the cold gas, leaving it unsettled and turbulent, thereby inhibiting its ability to collapse and form stars (see Ishibashi et al. 2014; Morganti 2017; Harrison et al. 2018). The differing nature of feedback processes governing these two populations may be responsible for their different evolutionary tracks. However, observational evidence is mixed, and it remains challenging to distinctly identify the relative importance of different feedback modes operating on various scales.

The classification of AGNs into HERGs and LERGs requires the measurement of flux densities for various optical emission lines. The most sophisticated criterion is based on the excitation index (EI),

$$\mathrm{EI} = \log([\mathrm{O\,III}]/\mathrm{H}\beta) - \frac{1}{3}[\log([\mathrm{N\,II}]/\mathrm{H}\alpha) + \log([\mathrm{S\,II}]/\mathrm{H}\alpha) + \log([\mathrm{O\,I}]/\mathrm{H}\alpha)], \quad (1)$$

utilizing four emission-line ratios (Buttiglione et al. 2010). As demonstrated by Buttiglione et al. (2010) for a sample of 113 local ($z < 0.3$) radio galaxies from the Third Cambridge Catalog of Radio Sources (3CR), an EI threshold of 0.95 divides radio galaxies into distinct populations of HERGs and LERGs. Naturally, obtaining reliable detections of all six emission lines needed for calculating the EI is often challenging. Therefore, a variety of classification mechanisms based on fewer lines have been devised, resulting in several large HERG and LERG catalogs in the literature. Among the most notable of these, with further details presented later in the paper, are the classifications of 18 286 and 6720 radio galaxies by Best & Heckman (2012) and Pracy et al. (2016), respectively.

Observations of H I 21-cm absorption lines can reveal the kinematics and distribution of cold atomic gas associated with HERGs and LERGs, providing an insight into the distinguishing features of these two populations. Chandola et al. (2020) found that H I 21-cm absorption detection rates among HERGs and LERGs depend crucially on the extent of the radio emission and the mid-infrared (MIR) colors measured by the Wide-field Infrared Survey Explorer (WISE; Wright et al. 2010; Cutri et al. 2021). Using a sample of 191 LERGs and 27 HERGs at $z < 0.25$, they found comparable H I 21-cm absorption detection rates between the two types when matched in radio size and WISE color ($60.6^{+16.8}_{-13.4}$% for LERGs and $50.0^{+26.9}_{-18.4}$% for HERGs). This suggests that at least a fraction of LERGs contain significant amounts of gas and dust. It is likely that in LERGs, this gas is more susceptible to feedback effects, hindering its transport to the vicinity of the central black hole. However, the evidence remains sparse due to considerable statistical uncertainties, and the existing samples have been limited to lower redshifts ($z < 0.25$; Maccagni et al. 2017).

In this paper, we use radio continuum images and spectra from the MeerKAT Absorption Line Survey (MALS; Gupta et al. 2018) to extend H I 21-cm line studies of radio galaxies to higher redshifts and lower radio luminosities. While previous surveys of H I absorption in LERGs and HERGs were limited to $z \lesssim 0.2$ (e.g., Chandola et al. 2020; Maccagni et al. 2017), the present work extends this redshift range to $z \sim 0.5$, thereby providing the highest-z sample of such galaxies studied to date. Section 2 presents the MALS data products and crossmatching with the Sloan Digital Sky Survey (SDSS) data release 18 (DR18) used to classify 1908 radio sources into HERGs and LERGs, employing a framework that combines multiple optical-emission line diagnostics. Section 3 presents the results of our H I 21-cm search in the sample of HERGs and LERGs, along with descriptions of new detections and their statistical properties. We also discuss the kinematics of the absorbing gas and its implications for inflow and AGN feedback. The results are summarized in Section 4. Throughout this paper, we adopt a Λ cold dark matter cosmology with Ω_m=0.315, Ω_Λ=0.685, and H_0=67.4 km s^{-1} Mpc^{-1} (Planck Collaboration VI 2020). Unless otherwise stated, all logarithms (log) are base 10.

2. Sample: HERGs and LERGs

This section details the crossmatching of MALS data release 1 (DR1) with SDSS DR18, and the HERG and LERG classification procedure using emission lines detected in the SDSS spectra.

2.1. MALS observations and data products

MALS observed 391 pointings in the L band (900–1670 MHz) during the first phase of the survey from 2020, April, 01 to 2021, January, 18. Gupta et al. (2022) present the details of a large spectroscopic campaign to define the survey footprint (see also Krogager et al. 2018). The MeerKAT data were processed using the Automated Radio Telescope Imaging Pipeline (ARTIP; Gupta et al. 2021), which is based on the NRAO Common Astronomy Software Applications (CASA) package (Team et al. 2022) to produce continuum images and spectral line cubes for 15 spectral windows (SPWs) covering the L band. The details of continuum images and the associated catalog of 715 760 unique radio sources detected at a signal-to-noise ratio (S/N) >5 are presented in the MALS DR1 paper (Deka et al. 2024b). Briefly, the median root mean square (rms) noise away from the pointing center is ∼20 μJy beam^{-1}, and the spatial resolution across the band is 8″–12″. The DR1 catalog includes spectral indices, α, where $S_\nu \propto \nu^\alpha$, based on the flux densities measured at 1006 MHz and 1381 MHz. The L-band spectra in the heliocentric frame used here to search for H I 21-cm absorption were extracted toward pixels corresponding to the peak flux density of the radio source. The absorption was searched within ±2000 km s^{-1} of the redshifted H I 21-cm line frequency following the methodology adopted for the MALS Galactic spectral line search (Gupta et al. 2025). Further details on the radio sources and their associated spectra are provided in subsequent sections.

2.2. Crossmatching with SDSS

We crossmatched the MALS DR1 catalog at 1006 MHz with the SDSS DR18 spectroscopic catalog using a search radius of 5″ to identify 1965 radio sources at $z < 0.5$, the redshift range suitable to search for H I 21-cm absorption using MeerKAT's L band. A matching radius of 2″ should be optimal for crossmatching

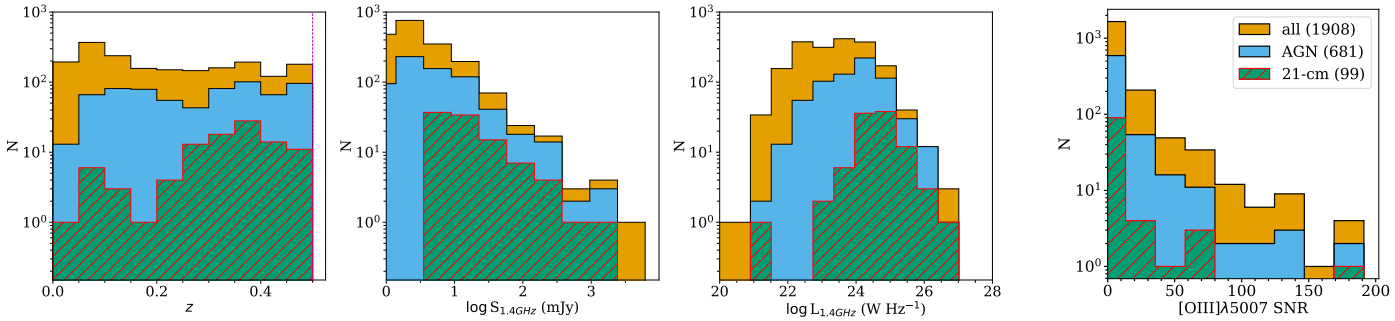


Fig. 1. Distribution of z (first panel), $S_{1.4\,GHz}$ (second), $L_{1.4GHz}$ (third), and S/N of [O III]λ5007 (fourth) for the initial sample of 1908 radio sources (yellow histograms). Of these, 681 are classified as AGNs (blue; see Sections 2.3 and 2.4 for details). Finally, 99 LERGs and HERGs from this subsample were searched for associated H I 21-cm absorption (hatched green; details in Section 3). The low-z deficit in the green histogram reflects the paucity of sources exceeding the 4 mJy flux density cut applied for the 21-cm absorption search.

with SDSS (Lu et al. 2007; Gupta et al. 2022). However, a 5″ radius was used to compensate for the large synthesized beam (12″) at 1006 MHz. This ensures that AGNs with extended radio morphologies, such as FRI and FRII sources, are not excluded. For 152 sources, the flux-weighted mean radio positions differed by more than 2″, even though the peak radio positions remained consistent within that threshold. To ensure a reliable crossmatched sample, we visually inspected all matches obtained from the Panoramic Survey Telescope and Rapid Response System (PanSTARRS; Chambers et al. 2016). Notably, the 152 sources with separations between 2″ and 5″ predominantly exhibited extended morphologies. However, in all but 57 cases, the optical source coincided with the position of the radio core, i.e., the radio component likely coincident with the AGN. After excluding these 57 spurious matches, our sample comprises 1908 sources. The first three panels of Fig. 1 show the distributions of redshift (z), 1.4 GHz flux density ($S_{1.4\,GHz}$) and luminosity at 1.4 GHz ($L_{1.4\,GHz}$) for the sample. We note that 53/1908 sources were not detected at 1380 MHz. For these 1006 MHz flux densities were scaled to 1.4 GHz using a typical spectral index of $\alpha = -0.7$.

2.3. Spectroscopic fitting using GELATO

The classification into LERGs and HERGs was carried out in two steps. In Section 2.4, we first use the Baldwin–Phillips–Terlevich (BPT) emission line diagnostic method (Baldwin et al. 1981) based on the location of the source in the [O III]/Hβ–[N II]/Hα plane, to distinguish radio sources as either AGN or star-forming (SF) galaxies. We also use Hα- line luminosity ($L_{H\alpha}$) and $L_{1.4\,GHz}$ for this purpose. Both these luminosities serve as independent measures of the star formation rate for SF galaxies. Conversely, for radio-loud AGNs, an excess of radio emission over that estimated from the Hα luminosity is expected. In the second step (Section 2.5), AGNs are classified into HERGs and LERGs. Notably, across $0 \leq z \leq 0.5$, the [O III]λ5007 line remains within the wavelength coverage of the SDSS spectra. Consequently, the classification of objects into LERGs and HERGs is feasible using one of the several criteria defined by Best & Heckman (2012), even though at the highest redshifts, the majority of other lines, including [N II]λ6583, [S II]$\lambda\lambda$6716, 6731, [O I]λ6300, and Hα, are beyond the SDSS coverage.

We used the Galaxy/AGN Emission-Line Analysis TOol[1] (GELATOv2.5.2; Hviding et al. 2022) to measure the emission line fluxes, the equivalent widths, and the associated uncertainties. For a given spectrum with an initial redshift estimate (z_0) accurate to at least 0.5%, GELATO fits a user-specified list of spectral lines to the input spectrum. The emission lines used in our analysis are summarized in Table 1. These are classified into two groups: narrow and Balmer. Emission-line species

[1] https://github.com/TheSkyentist/GELATO

Table 1. GELATO Emission Line Dictionary used in this work.

Species	Line λ_{air} (Å)	Ratio
Narrow Group		
[S II]	6716.44	–
	6730.82	–
[N II]	6583.45	1
	6548.05	0.34
[O I]	6300.30	1
	6363.78	0.333
He I	5875.62	–
[O III]	5006.84	1
	4958.91	0.35
	4363.21	–
[Ne III]	3868.76	–
[O II]	3726.03	–
	3728.82	–
[Ne V]	3425.88	–
Balmer Group		
H I	6562.79	–
H I	4861.28	–
H I	4340.47	–

Notes. Emission lines are grouped into species, and species into groups. Lines belonging to a given species (e.g., [S II]λ6716.44 and [S II]λ6730.82]) must share common kinematics; namely, redshift and velocity dispersion. Additional components, `Outflow` for [O III]and `Broad` for Balmer lines, and the constraints imposed on their kinematical properties are discussed in Section 2.3.

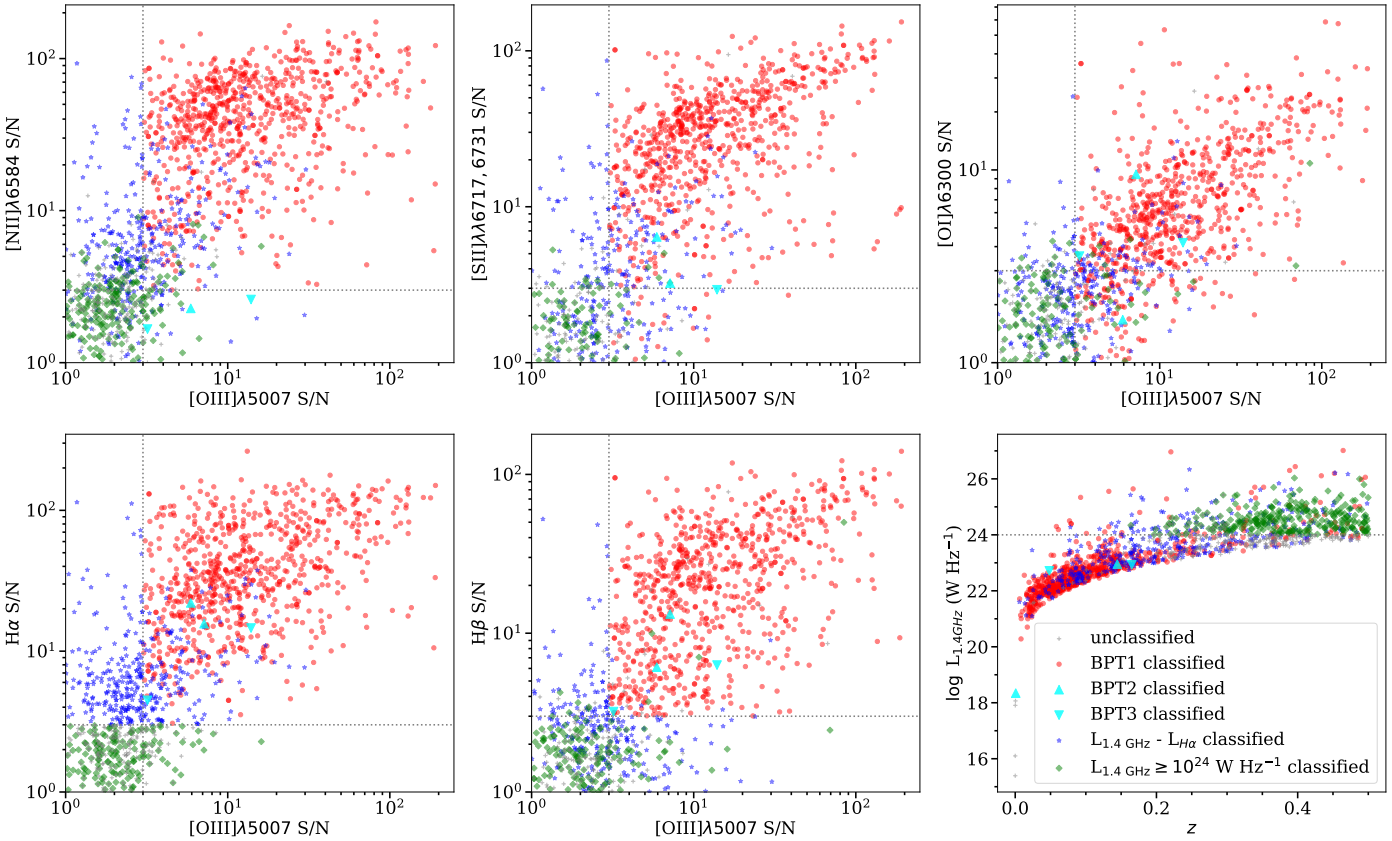


Fig. 2. S/N distribution of various lines used for AGN and SF classification, and the location of sources in the $L_{1.4\,GHz}$–z plane based on the classification method (details in Section 2.4). Sources with line S/N< 1 are not shown. The dashed vertical and horizontal lines denote an S/N = 3, except in the bottom right panel where the dashed horizontal line ($L_{1.4\,GHz} = 10^{24}$ W Hz^{-1}) marks the boundary segregating SF and AGN-dominated sources according to Pracy et al. (2016).

within their respective groups can optionally have their redshifts and velocity dispersions (σ) tied together. Following Hviding et al. (2022), both z and σ of species in the "Balmer" group are tied. Flux ratio constraints based on atomic physics are naturally enforced for all emission lines within a given species. For [O III] and Balmer lines, we also included the possibility of additional components designated as "outflow" and "broad", respectively. Such components, often associated with AGNs, do not share the z and σ values of their narrow counterparts. To avoid fitting physically unrealistic components, the line centroids (v_0) based on the redshifts (z_0) and dispersions (σ) of the Gaussian components were constrained to GELATO's predefined ranges[2]. These constraints are based on the emission line properties of large samples of quasars and galaxies from Mullaney et al. (2013), Shen et al. (2011), and Hao et al. (2005).

To model the underlying continuum emission, GELATO uses a trust region reflective (TRF; Branch et al. 1999) algorithm with a least-squares loss function to iteratively estimate the best-fitting parameters from an initial estimate of the model. After masking out a 10 000 km s^{-1} region around each specified spectral line, the continuum is modeled using simple stellar populations (SSPs) spanning a range of ages and metallicities from the Extended MILES stellar library (E-MILES; Vazdekis et al. 2016). To characterize the power-law emission originating from an unobscured AGN accretion disk, GELATO assesses whether the inclusion of a power-law component to the model leads to a substantial improvement in the fit. This validation is performed using an F test, affirming significance if the improvement is >3σ (a confidence level of ∼99.87%).

The GELATO fits revealed that an additional broad component to model the Hα emission is required for 643/1908 systems. In 123 of these cases, the dispersion of the broad component is close to the upper fitting bound (i.e., $\sigma \approx 6500$ km s^{-1}) and characterized by low S/N (<5 for 117/123). Typically, a S/N>5 is used to identify robust broad components (Escott et al. 2025). Adopting this threshold, we rejected broad components in these 117 sources and refit them using only narrow components. The distribution of the S/N of [O III]λ5007 from the final fits is shown in the last panel of Fig. 1. Since detection of this line is paramount for classifying sources into LERGs and HERGs (e.g., Tadhunter et al. 1998; Buttiglione et al. 2010; Best & Heckman 2012; Pracy et al. 2016), we discarded 375/1908 sources where the S/N([O III])< 1. Further details on the fit line parameters and examples of fits for the remaining 1533 radio sources are provided in the following sections.

2.4. Separating AGN and SF galaxies

We classified radio sources with the [O III]λ5007 line detected at S/N > 1 into either AGN or SF galaxies, predominantly utilizing the BPT diagnostic (Baldwin et al. 1981). Fig. 2 presents the

[2] For the narrow components, the limits are 60 km s^{-1} < σ < 500 km s^{-1} and v_0 within ±300 km s^{-1} from z_0. For the broad and outflow components, these restrictions are 1200 km s^{-1} < σ < 6500 km s^{-1} with v_0 within ±600 km s^{-1}, and 100 km s^{-1} < σ < 750 km s^{-1} and v_0 within [–750, +150] km s^{-1}, respectively.

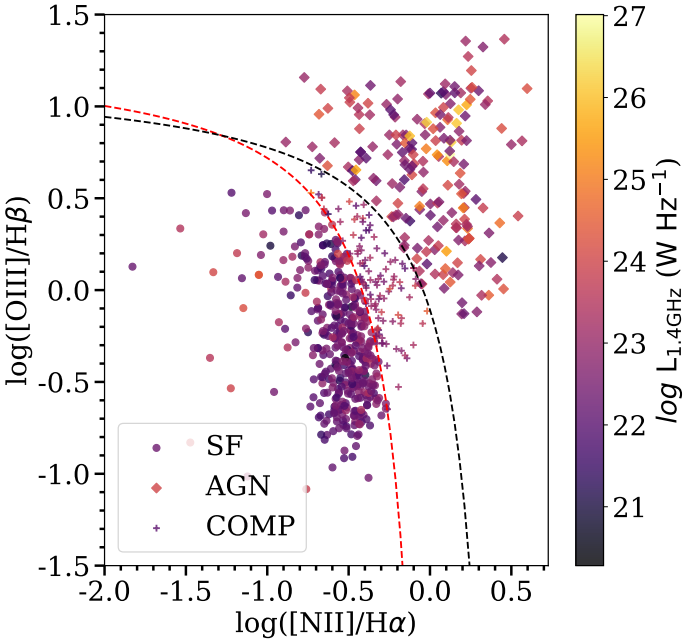


Fig. 3. BPT1 classified AGN, SF, and Composite (COMP) galaxies color-coded according to their 1.4 GHz radio luminosity ($L_{1.4\,GHz}$).

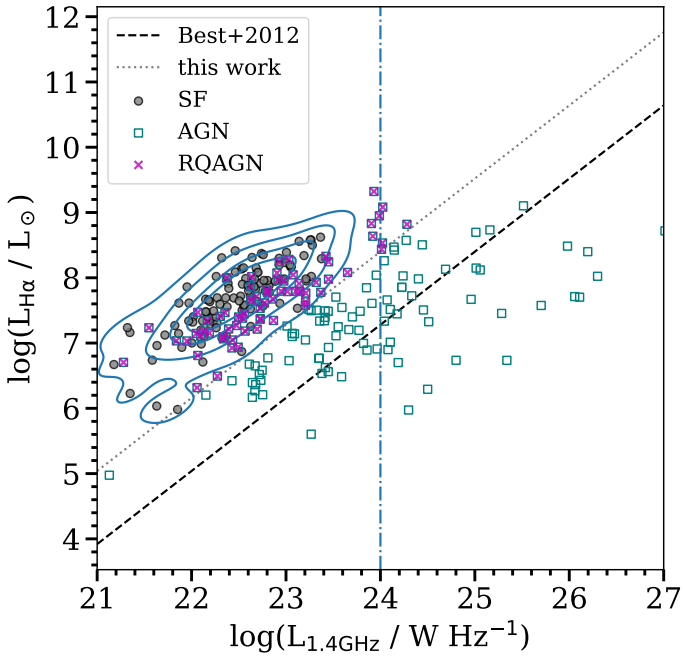


Fig. 4. BPT classified AGN and SF galaxies with only narrow Balmer lines in the $L_{H\alpha}$–$L_{1.4\,GHz}$ plane. The dashed line (black) marks the conservative division between AGN and SF galaxies from Best & Heckman (2012), and the contours correspond to SF galaxies. The dotted line represents the criteria used to exclude radio-quiet optical AGNs (RQAGNs). The vertical line marks the SF versus AGN division, where sources with $L_{1.4\,GHz} > 10^{24}$ W Hz^{-1} are classified as AGNs.

S/N distributions of various emission lines relevant for the classification. Based on the emission-line ratios alone (see Table 2 for a summary), 730 sources were classified into AGN (196), SF (426), or composite (108) galaxies. Except for three cases, the remaining are based on BPT1: [O III]/Hβ versus [N II]/Hα (see Fig. 3). BPT2 and BPT3 refer to the diagnostic diagrams of [O III]/Hβ versus [S II]/Hα and [O I]/Hα, respectively. These diagnostics classified one and two sources into SF and AGN categories, respectively.

In the remaining cases, not all four emission lines required for the BPT classification were reliably detected (S/N > 3) or covered within the wavelength range of the SDSS spectra. To classify these sources, we employed the $L_{H\alpha}$ versus $L_{1.4\,GHz}$ diagnostic plane. Both Hα and 1.4 GHz radio continuum luminosities serve as independent measures of the star formation rate in SF galaxies, creating a well-defined correlation (Hopkins et al. 2003; Best & Heckman 2012; Duncan et al. 2020). Conversely, for radio-loud AGNs, a significant excess of radio emission over that estimated from the Hα luminosity is expected. To formally separate these populations, Best & Heckman (2012) utilized a conservative division line defined by $\log(L_{H\alpha}/L_\odot) = 1.12 \times (\log L_{1.4\,GHz}(\mathrm{W\,Hz^{-1}}) - 17.5)$. Fig. 4 depicts our BPT-classified AGN and SF galaxies on this plane. Interestingly, a significant fraction of BPT classified AGNs lie in the SF region in this diagram, implying that in these sources the radio emission is predominantly due to star formation rather than AGN activity. This, however, does not apply to broad-lined objects, where the Hα luminosity mainly originates from the AGN broad line region (BLR) rather than star formation. Consequently, we restricted this planar analysis to systems with only narrow Balmer lines (Fig. 4). The distribution of SF galaxies, shown as contours in Fig. 4, suggests that an alternative division line (dotted), defined by $\log(L_{H\alpha}/L_\odot) = 1.12 \times (\log L_{1.4\,GHz}(\mathrm{W\,Hz^{-1}}) - 16.5)$, encapsulates the SF population more realistically. Using this modified division line, we first excluded 68 narrow-lined radio-quiet optical AGNs from the sample. Applying this same criterion to the aforementioned sources lacking full BPT coverage, we classified 346 sources into 261 AGNs and 85 SF galaxies.

Table 2. Summary of classification of 1300 out of 1533 sources with [O III] detected at S/N>1 into AGN, SF, or composite galaxies (233 sources remain unclassified).

Classification method	SF	AGN	Composite
BPT1	425	194$^{(\dagger)}$	108
BPT2	1	0	0
BPT3	0	2	0
$L_{1.4\,GHz}$ versus $L_{H\alpha}$	85	261	–
$L_{1.4\,GHz} > 10^{24}$ W Hz^{-1}	–	224	–

Notes. Table B.1 presents the full sample. $^{(\dagger)}$ Includes 68 radio-quiet AGNs with only narrow Balmer lines.

Of the remaining 457/1533 that could not be classified using any of the above methods, we classified 224 with luminosities exceeding $L_{1.4\,GHz} > 10^{24}$ W Hz^{-1} as AGNs, since such high luminosities would require unrealistically large star formation rates to be powered by star formation alone (e.g., Pracy et al. 2016; Murphy et al. 2011). The bottom right panel of Fig. 2 shows the location of sources in the $L_{1.4\,GHz}$–z plane based on the classification method. Evidently, most sources at higher redshifts are classified using the $L_{1.4\,GHz}$ criterion. Finally, 233 sources remain unclassified. We excluded these from further analysis. In summary, 1300 out of 1533 sources were classified into one of the following categories: AGN (681), SF (511), or composite (108) galaxies (Table 2). The full MALS-SDSS catalog is provided in Table B.1.

2.5. AGN classification into LERGs and HERGs

Here we classify the 613 radio-loud AGNs, obtained after excluding 68 radio-quiet sources from the 681 AGNs identified in the previous section, into LERGs and HERGs using the following set of diagnostics from Best & Heckman (2012).

1. A source is a HERG (LERG) if all six emission lines, [O III], [N II], [S II], [O I], Hα, and Hβ, are detected, and EI > 0.95 (EI < 0.95) by at least 1σ. Typical HERG and LERG spectra classified using this method (`Diagnostic 1`) are shown in Fig. A.2.
2. If only four out of six above-mentioned lines are detected, classification is determined at >1σ significance using the diagnostics (`Diagnostic 2`) of Kewley et al. (2006)[3] (see Fig. A.3 for representative spectra).
3. Classification is based on the rest equivalent width (REW) of [O III] > 5Å (HERG) or < 5Å (LERG) at 1σ significance (`Diagnostic 3`; see Fig. A.4 for representative spectra).
4. (1) − (3) are repeated, but without applying the 1σ criterion (`Diagnostic 4`).
5. For weak line galaxies with [O III], [N II] and Hα detections at >1σ, we apply the diagnostics of Cid Fernandes et al. (2010)[4] based on [O III]/Hα and [N II]/Hα ratios (`Diagnostic 5`; see Fig. A.5 for representative spectra).

Usually, these five diagnostics are applied in a preferential order to classify narrow-line AGNs (e.g., Buttiglione et al. 2010; Best & Heckman 2012). Rather than applying the five diagnostics sequentially, as in Best & Heckman (2012), we applied all diagnostics simultaneously and combined their output using a weighted framework to obtain a more robust classification. To achieve this, we introduced a confidence measure (C) and a reliability factor (R) to quantify data quality and the intrinsic strength of each diagnostic. The final significance (S) of a source's classification is then the weighted average of all available diagnostics, $S = \frac{\sum_{i=1}^{5} R_i \cdot C_i}{\sum_{i=1}^{5} R_i}$. Note that we assign a negative sign for LERGs and a positive sign for HERGs. This framework assigns a continuous, interpretable significance score, where $|S| \in [0, 1]$.

The details of calculations of C and R are provided in Appendix A. We evaluated various weighting schemes to calculate S, ultimately adopting $R_1 = 1$, $R_2 = R_3 = 0.9$, $R_4 = 0.8$, and $R_5 = 0.5$ for AGNs fit using only narrow components. For the 82 AGNs requiring an additional broad Hα component with integrated S/N > 5, the criterion of EI = 0.95 (`Diagnostic 1`) is inapplicable. For these we set $R_1 = 0$. From the narrow-only and narrow+broad subsets, we identified 58 HERGs and 318 LERGs, and 41 HERGs and 9 LERGs, respectively. The prevalence of HERGs (82%) among AGNs with broad Balmer components is consistent with the findings of Buttiglione et al. (2010). In summary, starting with 613 AGNs with 531 (narrow-only) + 82 (narrow+broad) AGNs, we classified a total of 426 AGNs into 99 HERGs and 327 LERGs. The remaining 187 sources could not be classified due to a lack of emission lines satisfying the S/N criteria. Note that the initial subset of 613 AGNs still included 82 sources with a broad Hα component. For these the AGN activity cannot be unambiguously confirmed but the contamination is too small to affect the statistical results presented here.

[3] In the [O III]/Hβ vs [S II]/Hα diagnostic, the classification follows $\log([\mathrm{O\,III}]/\mathrm{H}\beta) \lesssim 1.89 \log([\mathrm{S\,II}]/\mathrm{H}\alpha) + 0.76$ for LERGs and HERGs, respectively. For the [O III]/Hβ vs [O I]/Hα diagnostic, the respective classification is $\log([\mathrm{O\,III}]/\mathrm{H}\beta) \lesssim 1.18 \log([\mathrm{O\,I}]/\mathrm{H}\alpha) + 1.30$.

[4] The classification follows $\log([\mathrm{O\,III}]/\mathrm{H}\alpha) \lesssim 1.20 \log([\mathrm{N\,II}]/\mathrm{H}\alpha) - 0.15$ for LERGs and HERGs, respectively.

Table 3. Statistical comparison between LERG (327) and HERG (99) samples.

Parameter	Median LERG	Median HERG	KS test p value
$\alpha_{1.0}^{1.4}$	−0.62 ± 0.29	−0.77 ± 0.20	0.002
$\log \mathrm{L}_{1.4\,\mathrm{GHz}}$ (W Hz^{-1})	24.04 ± 0.51	24.01 ± 0.81	0.04
$S_{1.0\,\mathrm{GHz}}$ (mJy)	5.07 ± 3.33	4.53 ± 2.94	0.3
z	0.27 ± 0.10	0.24 ± 0.15	0.007
$g - r$ (k-corrected)	0.85 ± 0.04	0.76 ± 0.09	3.3×10^{-15}

Notes. The reported uncertainties are the median absolute deviations (MADs).

For a consistency check, we crossmatched our MALS-SDSS sample of 426 HERGs and LERGs with Best & Heckman (2012) and found 43 common sources. Due to the choice of weights, R_i, we find an excellent agreement, as only one source shows classification mismatch: J144017.88+055630.1, which is a LERG in Best & Heckman (2012), but a HERG ($S = 0.42$) in our weighting-based classification scheme. Additionally, 41 sources are common with Pracy et al. (2016). There are three mismatches: J094319.09−000423.7, J145322.99+045802.6, and J015517.11+002741.4. In our scheme, J094319.09−000423.7 is a borderline LERG (EI = 0.85±0.04; $S \sim -0.33$). However, its spectrum shows a strong [O III] λ5007 line (REW = 89.9±2.3 Å) and a weak 4000 Å break, indicating HERG-like features. Similarly, J145322.99+045802.6 is also a borderline LERG (EI = 0.89±0.05; $S \sim -0.01$) with a strong [O III] λ5007 line (REW = 54.0±3.9 Å) and a weak 4000 Å break. J015517.11+002741.4 is a HERG in our classification scheme with EI = 1.11±0.07 and $S = 0.59$, while it is a LERG in Pracy et al. (2016). We do not reclassify these marginal mismatches.

2.6. Properties of HERGs and LERGs

Fig. 5 compares HERGs and LERGs in terms of spectral indices ($\alpha_{1.0}^{1.4}$), radio luminosity ($\mathrm{L}_{1.4\mathrm{GHz}}$), flux density at 1.0 GHz ($\mathrm{S}_{1.0\mathrm{GHz}}$), redshift, and k−corrected[5] optical color ($g - r$). The statistics and KS-test p values in Table 3 show that LERGs and HERGs differ by $\gtrsim 3\sigma$ in $\alpha_{1.0}^{1.4}$ and optical colors, with no significant difference in $S_{1.0\,\mathrm{GHz}}$. Notably, while LERGs show a slightly higher median $\log \mathrm{L}_{1.4\mathrm{GHz}}$, HERGs span the full luminosity range (Fig. 5, second panel). The two populations also differ at >2σ in redshift, with LERGs distributed at higher median z. These differences in $\mathrm{L}_{1.4\,\mathrm{GHz}}$ and z are primarily driven by the selection effects discussed in Section 2.4. The only astrophysically meaningful differences are observed in spectral index and optical $g - r$ color. The slightly steeper median $\alpha_{1.0}^{1.4}$ for HERGs likely reflects their association with FRII-type, lobe-dominated radio galaxies, whereas LERGs comprise both FRI and FRII types (Buttiglione et al. 2010; Best & Heckman 2012; Heckman & Best 2014). A more pronounced difference (>3σ) is seen in k−corrected optical $g - r$ color. The LERGs are significantly redder, reflecting older, more massive, and less star-forming host galaxies. This confirms the finding of Best & Heckman (2012) that LERGs have redder optical colors than HERGs of the same radio luminosity, here extended to a broader luminosity range ($\log \mathrm{L}_{1.4\,\mathrm{GHz}}$ (W Hz^{-1}) ∼ 21.1–27.0) and higher redshifts ($z < 0.5$).

In Fig. 6, we show the distribution of redshift, 1.4 GHz radio luminosity, and k-corrected $g - r$ color for $\mathrm{L}_{1.4\mathrm{GHz}}$-matched MALS and Best & Heckman (2012) samples. The k-corrected

[5] Following the methodology of Chilingarian et al. (2010).

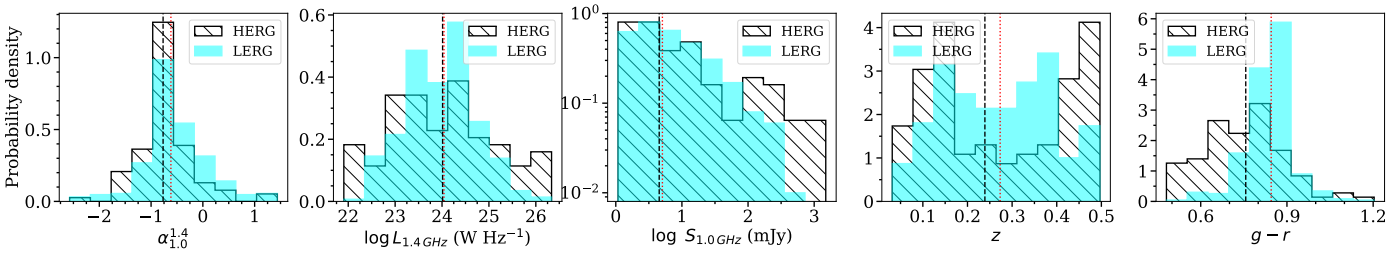


Fig. 5. Distribution of $\alpha_{1.0}^{1.4}$ (first), $L_{1.4GHz}$ (second), $S_{1.0GHz}$ (third), z (fourth), and k-corrected $g-r$ (fifth) for the LERG and HERG samples. The dashed red and black lines mark the median values for LERGs and HERGs, respectively.

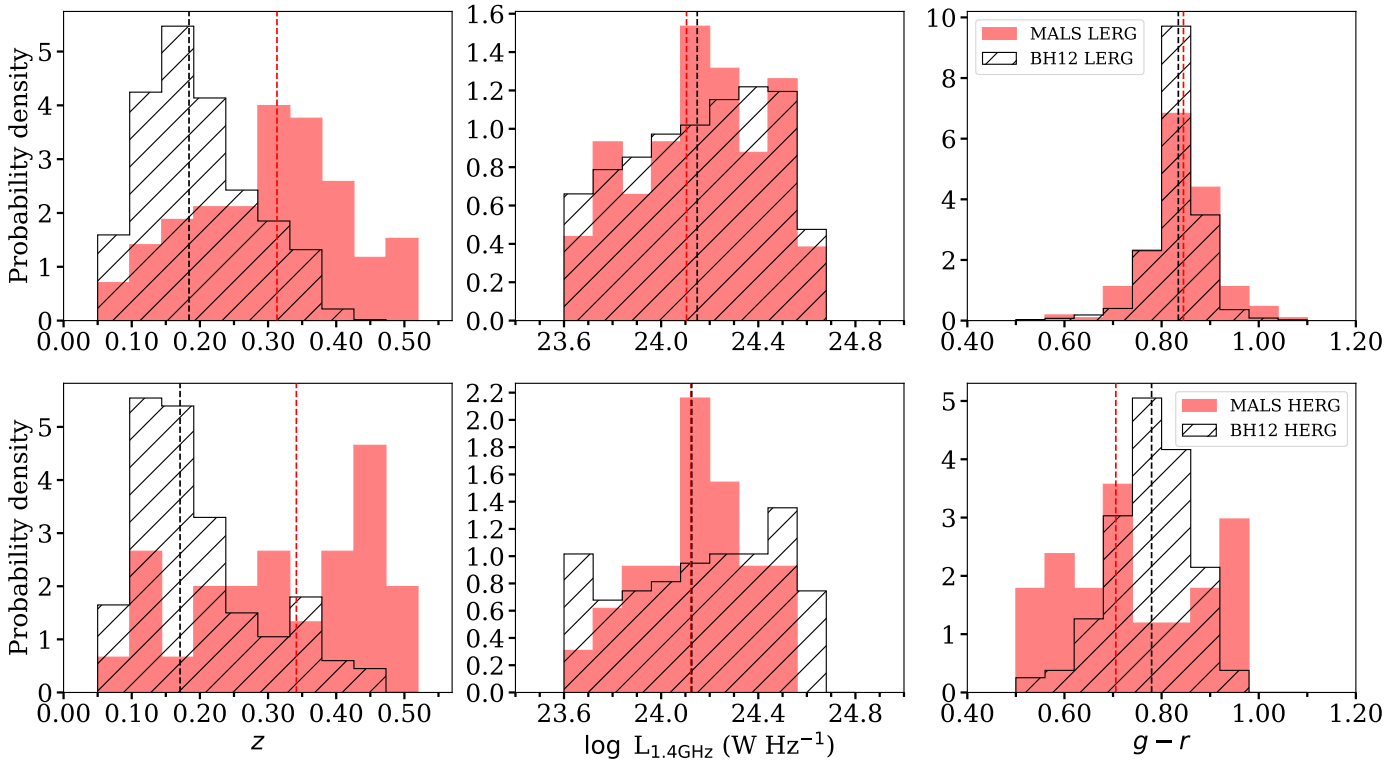


Fig. 6. Histograms comparing the distributions of z, $L_{1.4\,GHz}$, and k-corrected $(g-r)$ for LERGs (top panel) and HERGs (bottom panel), using the MALS and Best & Heckman (2012) samples matched in $L_{1.4\ GHz}$.

$g-r$ colors are consistent for the LERGs at $p = 0.05$ level, while the marginal $<3\sigma$ ($p = 0.003$) discrepancy for HERGs is likely an artifact of small-number statistics in the MALS subset ($N = 32$). To compare the LERG fractions between the MALS and Best & Heckman (2012) samples objectively, we matched the datasets in both redshift and $L_{1.4,GHz}$. The samples were partitioned at the median redshift of the MALS sample, and the low- and high-z bins were analyzed independently. From Fig. 7, in the low-z bin, the The LERG fractions are $92.0^{+5.2}_{-9.6}\%$ for MALS and $97.9 \pm 0.3\%$ for BH12 (binomial uncertainties), representing only a $\sim 1\sigma$ difference. In the high-z bin, the fractions are $95.2^{+3.9}_{-10.1}\%$ (MALS) and $97.4 \pm 0.6\%$ (BH12), which are again statistically consistent. To conclude, we find no statistically significant evidence for a redshift dependence in the LERG fraction between the two matched samples.

3. H I 21-cm absorption search

We selected 99 radio sources ($S_{1.4\ GHz} > 4$ mJy) with usable spectra from the 426 MALS-SDSS sample of LERGs and HERGs at $z_{em} < 0.5$ for an H I 21-cm absorption line search. This subset comprises 79 LERGs and 20 HERGs. Of these, 22 were classified as AGNs using BPT1, 36 using the $L_{H\alpha}$–$L_{1.4\,GHz}$ criteria, and 41 based on $L_{1.4\,GHz} > 10^{24}$ W Hz^{-1}. The sample spans nearly six decades in radio luminosity and reaches flux densities an order of magnitude fainter than any prior targeted H I survey. Following the absorption line search methodology of Gupta et al. (2025), we detected five absorbers. The resulting absorption profiles presented in Fig. 8 exhibit widths spanning ~100 to ~1000 km s^{-1}(see Table 4 for details). Notably, three absorbers are entirely redshifted with respect to z_{em}, likely tracing infalling gas (van Gorkom et al. 1989), which can be triggered by merger activity (see the discussion of J0943−0004 in Section 3.1.2). Below, we first discuss the properties of detections in detail and then the statistical properties of the overall sample, including H I absorption nondetections.

3.1. Properties of detections

3.1.1. Kinematics of the absorbing gas

To characterize the gas kinematics, we used the velocity shift of the absorption peak (V_{peak}) relative to z_{em}, the full width between nulls (FWBN) indicated by the shaded velocity range in Fig. 8, and the velocity-integrated optical depth ($\int \tau\, dv$). Asymmetries

Table 4. Details of H I 21-cm absorption detections.

MALS ID	z_{em}(opt)	z_{abs}	Δv (km s^{-1})	σ_{rms} (mJy beam^{-1})	FWBN (km s^{-1})	S_{norm} (mJy)	$\int \tau\, dv$ (km s^{-1})	N(H I) (cm^{-2})	Class
(1)	(2)	(3)	(4)	(5)	(6)	(7)	(8)	(9)	(10)
J022836.49−010720.8	0.47115	0.46977	8.1	0.8	880	231.4	12.0±0.3	(22.2±0.3)×10^{20}	HERG
J094319.09−000423.7	0.46435	0.46650	8.1	1.9	122	734.5	0.27±0.07	(49±9)×10^{18}	LERG
J101024.28+153929.9	0.28620	0.28781	7.1	0.9	214	14.1	21±2	(37±3)×10^{20}	LERG
J111736.77−023544.0	0.47290	0.47096	8.1	1.2	324	757.3	0.62±0.08	(11.2±0.8)×10^{19}	LERG
J145556.40+044150.0	0.34714	0.34988	7.4	0.8	220	17.2	13±1	(24±2)×10^{20}	LERG

Notes. Column 1: MALS-SPW2 source ID. Column 2: optical spectroscopic redshift from SDSS. Column 3: Redshift corresponding to absorption peak. Column 4: velocity resolution at the redshifted 21-cm line frequency. Column 5: unsmoothed spectral rms. Column 6: full width between nulls (FWBN) of the absorption profile. Column 7: flux density used to normalize the spectrum. Column 8: Velocity integrated optical depth. Column 9: column density estimated assuming $T_s = 100$ K and $f_c = 1$. Column 10: optical spectroscopic classification.

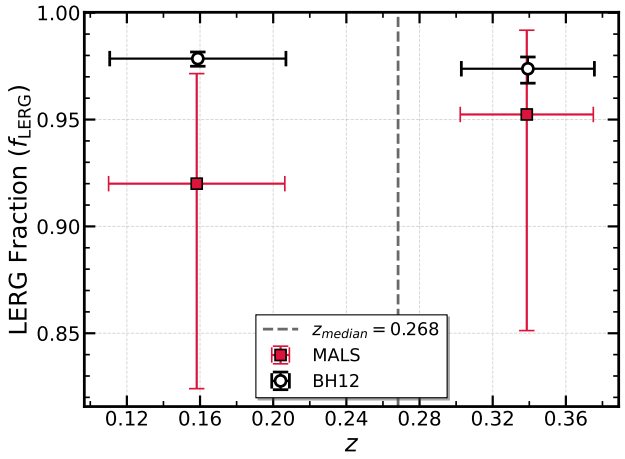


Fig. 7. Comparison of LERG fractions between the BH12 (Best & Heckman 2012) and MALS samples, evaluated within two redshift bins. Horizontal error bars denote the width of each redshift bin, while vertical error bars represent the binomial uncertainties on the derived fractions.

in the absorption profiles were quantified using the parameter

$$A_p = \frac{\left|(\int \tau\, dv)_{Blue} - (\int \tau\, dv)_{Red}\right|}{(\int \tau\, dv)_{Total}}, \quad (2)$$

where $(\int \tau\, dv)_{Blue}$ and $(\int \tau\, dv)_{Red}$ represent the velocity-integrated optical depths of the profile blueward and redward of $V_{\rm peak}$, respectively. Normalization by the total integrated optical depth, $(\int \tau\, dv)_{Total}$, allows a uniform comparison across profiles with varying strengths. This formulation is mathematically analogous to the 1D profile asymmetry metrics commonly employed in HI emission studies to quantify spectral lopsidedness (e.g., Hank et al. 2025; Perron-Cormier et al. 2025). The first three panels of Fig. 9 present the distributions of FWBN, $|V_{\rm peak}|$ and A_p as a function of $L_{1.4\rm GHz}$ over 10^{24-27} W Hz^{-1}. Kendall-tau correlation tests show no significant trends among these parameters. This is consistent with an earlier finding of Deka et al. (2024a) in a sample of 19 H I 21-cm absorbers associated with radio galaxies ($L_{1.4\rm GHz} > 10^{26}$ W Hz^{-1}). Similarly, no significant correlation is observed between $V_{\rm peak}$ and A_p (Fig. 9, last panel). Among LERGs, we find a wide range in A_p (0.07–0.65) and significant velocity offsets from $z_{\rm em}$ (>350 km s^{-1}), indicative of kinematically disturbed absorbing gas, possibly driven by jet-ISM interaction. This is consistent with studies of more powerful ($L_{1.4\rm GHz} \sim 10^{23}$–$10^{26}$ W Hz^{-1}) and lower-redshift ($z < 0.2$) HERG and LERG samples (e.g. Glowacki et al. 2017; Chandola et al. 2020). Due to the single HERG detection in our sample, a robust kinematic comparison between the two classes is currently not feasible. Additionally, none of our five direct H I detections required broad optical emission-line components indicative of ionized outflows, preventing a direct multiphase comparison between unsettled ionized gas and H I properties.

3.1.2. Radio morphology

Radio morphology may provide a further insight into the origin of the observed H I kinematics. Two notable examples are the LERGs J0943−0004 and J1455+0441. In both cases, the radio emission is extended and the absorbing gas appears to be "infalling" relative to the systemic redshift. The MALS image of J0943−0004 displays a dominant "core" and diffuse lobes spanning ∼47 kpc, with the absorption against the radio core. The optical spectrum of this source exhibits double-peaked [O III] $\lambda\lambda$4959, 5007 emission lines symmetrically displaced around the systemic redshift, which is a strong indicator of ongoing merger activity or a dual AGN (Dutta et al. 2019). Furthermore, Pan-STARRS images (Fig. C.1) reveal a nearby companion galaxy at a projected separation of ∼5″ (∼30 kpc). Therefore, the observed infalling gas in J0943−0004 is likely merger-driven, with the interaction funneling gas toward the center (e.g., Barnes & Hernquist 1991, 1996; Hopkins et al. 2006). In contrast, the absorption toward J1455+0441 is detected against a hotspot located asymmetrically near the AGN. This potentially represents gas associated with a faint companion galaxy.

For the remaining three cases, the radio emission is unresolved at the MALS angular resolution. However, at VLBI scales, J0228−0107 reveals two components at 4.4 GHz, but it is unclear whether these represent a core-jet structure or a pair of lobes. J1010−1539 exhibits a core-jet morphology at 4.8 GHz, while J1117−0235 shows a complex morphology with multiple components possessing steep spectral indices based on images at 4.8 and 2.3 GHz. Both J0228−0107 and J1117−0235 show well-detached, blueshifted absorption components. In fact, the bulk of absorption in the five sources is completely blue or redshifted. Future VLBI spectroscopy and high-resolution

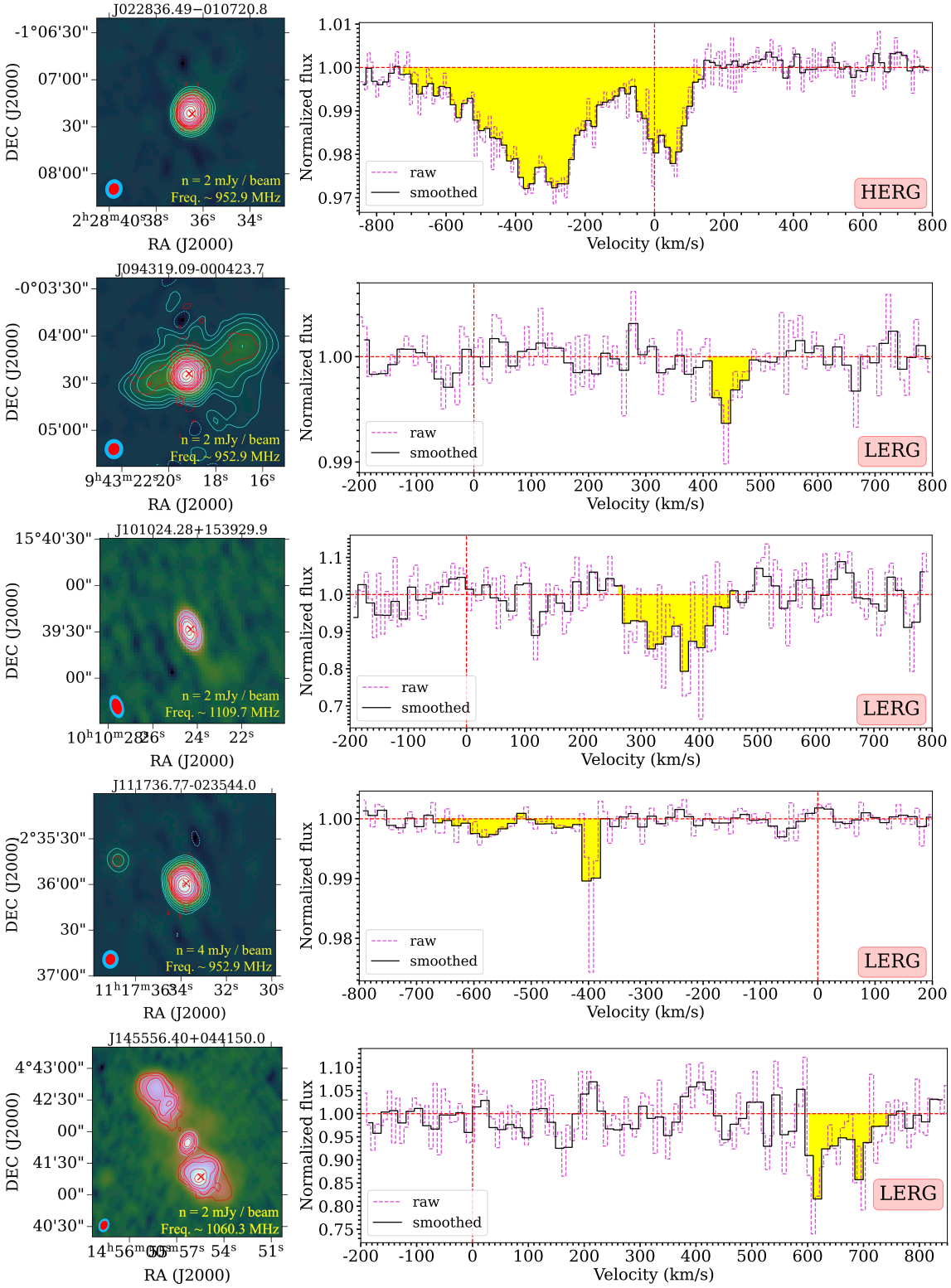


Fig. 8. The radio continuum images (left) and normalized absorption profiles (right) for the five sources listed in Table 4. The zero velocity corresponds to the optical redshift (z_{em}). Cyan contour levels at $n\times$ [–1, 1, 2, 4, 8, 16, ...]) represent the background continuum near the redshifted 21-cm line frequency. The corresponding n values and the image frequency are provided within the respective panels. Red contours denote the highest-resolution MALS L-band images (1643.0 MHz), with n values of 0.5, 5, 1.5, 4, and 0.3 mJy beam^{-1}, respectively. Filled cyan and red ellipses (bottom left) indicate the restoring beams for the background and high-resolution images, respectively. Spectra were smoothed with a 3-pixel Boxcar and decimated by a factor of two. Shaded velocity ranges correspond to the integrated optical depth ($\int \tau\, dv$) values listed in Table 4.

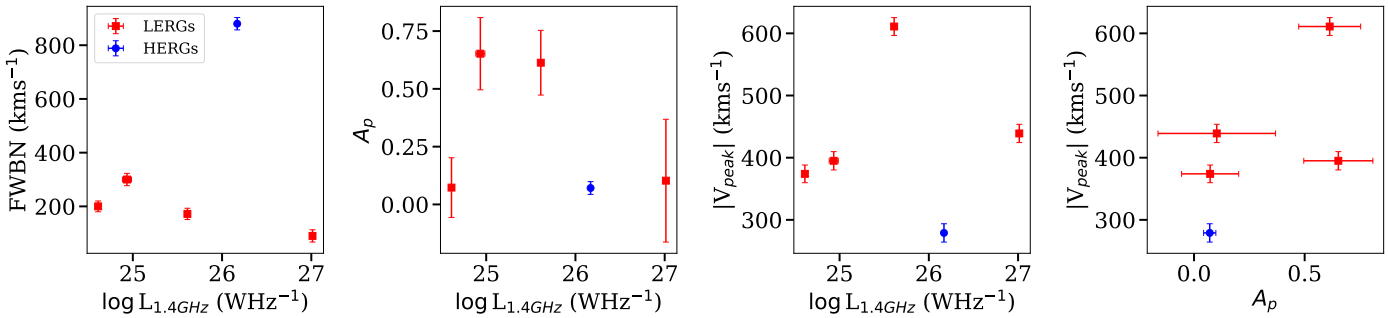


Fig. 9. Distributions of absorption line properties for the five detections. FWBN denotes the full width between nulls (FWBN) in km s^{-1}, A_p measures the asymmetry of the line profile, and $|V_{peak}|$ represents the shift of the absorption peak from z_{em}. The median uncertainty in log $L_{1.4\,GHz}$ is 0.003 dex, and is not visible at the scale of the figure.

Table 5. Detection rates for the MALS and Maccagni et al. (2017) samples.

Optical depth cutoff (km s^{-1})	Number of* sight lines	Number of** Detections	Percentage	Number of* sight lines	Number of** Detections	Percentage	Number of* sight lines	Number of** Detections	Percentage
		HERGs			LERGs			combined	
MALS sample: 79 LERGs, 20 HERGs									
0.1	2	1 (1)	50^{+50}_{-41} (50^{+50}_{-41})	2	2 (0)	100^{+0}_{-65} (0^{+92}_{-0})	4	3 (1)	75^{+25}_{-41} (25^{+58}_{-21})
0.2	2	1 (1)	50^{+50}_{-41} (50^{+50}_{-41})	3	2 (0)	67^{+33}_{-43} (0^{+61}_{-0})	5	3 (1)	60^{+40}_{-33} (20^{+46}_{-17})
0.3	3	1 (1)	33^{+67}_{-28} (33^{+67}_{-28})	4	1 (0)	25^{+58}_{-21} (0^{+46}_{-0})	7	2 (1)	29^{+38}_{-19} (14^{+33}_{-12})
0.5	4	1 (1)	25^{+58}_{-21} (25^{+58}_{-21})	4	1 (0)	25^{+58}_{-21} (0^{+46}_{-0})	8	2 (1)	25^{+33}_{-16} (13^{+29}_{-10})
1.0	5	1 (1)	20^{+46}_{-17} (20^{+46}_{-17})	7	0 (0)	0^{+26}_{-0} (0^{+26}_{-0})	12	1 (1)	8^{+19}_{-7} (8^{+19}_{-7})
5.0	14	1 (1)	7^{+16}_{-6} (7^{+16}_{-6})	50	2 (2)	4^{+5}_{-3} (4^{+5}_{-3})	64	3 (3)	5^{+5}_{-3} (5^{+5}_{-3})
10.0	18	1 (1)	6^{+13}_{-5} (6^{+13}_{-5})	68	2 (2)	3^{+4}_{-2} (3^{+4}_{-2})	86	3 (3)	3^{+3}_{-2} (3^{+3}_{-2})
Maccagni et al. (2017) sample: 170 LERGs, 15 HERGs									
0.1	2	1 (1)	50^{+50}_{-41} (50^{+50}_{-41})	7	3 (3)	43^{+42}_{-23} (43^{+42}_{-23})	9	4 (4)	44^{+35}_{-21} (44^{+35}_{-21})
0.2	3	1 (1)	33^{+67}_{-28} (33^{+67}_{-28})	14	7 (6)	50^{+27}_{-18} (43^{+26}_{-17})	17	8 (7)	47^{+23}_{-16} (41^{+22}_{-15})
0.3	4	2 (2)	50^{+50}_{-32} (50^{+50}_{-32})	21	7 (6)	33^{+18}_{-12} (29^{+17}_{-11})	25	9 (8)	36^{+16}_{-12} (32^{+16}_{-11})
0.5	8	4 (4)	50^{+40}_{-24} (50^{+40}_{-24})	54	13 (10)	24^{+9}_{-7} (19^{+8}_{-6})	62	17 (14)	27^{+8}_{-7} (23^{+8}_{-6})
1.0	12	4 (4)	33^{+26}_{-16} (33^{+26}_{-16})	117	25 (22)	21^{+5}_{-4} (19^{+5}_{-4})	129	29 (26)	23^{+5}_{-4} (20^{+5}_{-4})
5.0	15	3 (3)	20^{+20}_{-11} (20^{+20}_{-11})	168	25 (21)	15^{+4}_{-3} (13^{+3}_{-3})	183	28 (24)	15^{+4}_{-3} (13^{+3}_{-3})
10.0	15	2 (2)	13^{+18}_{-9} (13^{+18}_{-9})	170	13 (12)	8^{+3}_{-2} (7^{+3}_{-2})	185	15 (14)	8^{+3}_{-2} (8^{+3}_{-2})

Notes. The bracketed values represent absorbers with an integrated optical depth S/N > 8 (details in Gupta et al. 2025). The Poisson uncertainties in the detection rates were estimated following Gehrels (1986). Both samples are scaled to a common velocity resolution of 20 km s^{-1} and integrated optical depth sensitivities were calculated assuming a Gaussian line with FWHM = 20 km s^{-1}. * number of sight lines with a 3σ integrated optical depth sensitivity better than optical depth cutoff; ** number of detections with $\int \tau\, dv >$ optical depth cutoff.

molecular line observations will be essential to reveal the origin of the absorbing gas (see Combes & Gupta 2024).

3.2. Statistical properties

The search within ±2000 km s^{-1} of the redshifted H I 21-cm line frequency yielded five detections from the sample of 99 radio loud AGNs (79 LERGs and 20 HERGs). This corresponds to a detection rate of ∼5%, uncorrected for completeness or the varying optical depth sensitivity across the spectra. The associated absorbers generally exhibit broad line widths of ∼100 km s^{-1}, though their widths span a wide range where narrow lines (FWHM∼20 km s^{-1}) are also occasionally observed (e.g., Gupta et al. 2006; Maccagni et al. 2017; Aditya & Kanekar 2018b). Based on the completeness analysis in Gupta et al. (2025, their Fig. 7), the completeness fraction for injected absorbers with σ = 8 km s^{-1} (FWHM ∼ 18.9 km s^{-1}) at peak S/N > 6 (integrated S/N > 8) is near-unity. Notably, four of the five detections reported here have an integrated S/N > 8; the exception is J0943−0004 (integrated S/N = 4). Adopting 20 km s^{-1} as line width for nondetections, we estimate detection rates for a range of 3σ integrated optical depth cutoff limits over 0.1–10 km s^{-1} (see Table 5). Throughout this section, the uncertainties on the detection rates represent Poisson errors calculated following Gehrels (1986). Clearly, the detection rates for HERGs and LERGs agree within uncertainties.

Fig. 10 (top row) shows optical depth measurements versus 1.4 GHz luminosity and redshift for the MALS sample.

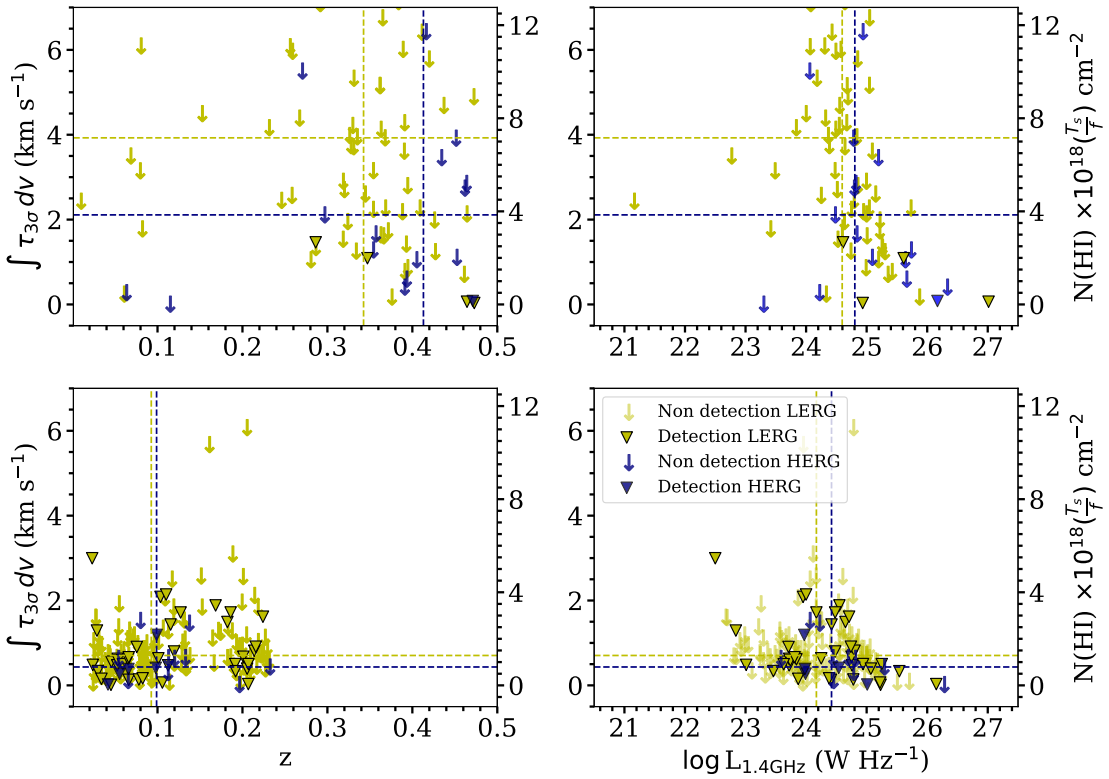


Fig. 10. Top row: MALS sources. Bottom row: 185 (170 LERGs, 15 HERGs) sources from Maccagni et al. (2017). The legends are the same across all panels. Vertical and horizontal dashed lines are median values. For better visibility 22 MALS sources (19 LERGs, 4 HERGs) are excluded from the panels with $\int \tau_{3\sigma}\, dv > 7$ km s^{-1}.

Splitting the sample at the median, the detection rates for the cutoff $\int \tau_{3\sigma}\, dv < 10$ km s^{-1} in the low and high bins are: $L_{1.4\,GHz}$ – $2.3^{+5.3}_{-1.9}$% (1/43) and $9.3^{+7.3}_{-4.4}$% (4/43); redshift – $4.6^{+6.1}_{-3.0}$% (2/43) and $7.0^{+6.8}_{-3.8}$% (3/43). While consistent within uncertainties, notably there is a skew in detections toward high $L_{1.4\,GHz}$. The high-$L_{1.4\,GHz}$ bin is significantly (>3σ) more sensitive (median $\int \tau_{3\sigma}\, dv = 2.1$ km s^{-1} versus 4.2 km s^{-1} in the low bin), and accounts for 4/5 detections.

The bottom row of Fig. 10 shows measurements from the survey by Maccagni et al. (2017) using the Westerbork Synthesis Radio Telescope (WSRT). These measurements have been scaled uniformly for a velocity resolution of 20 km s^{-1}. Before the comparison, we note that the WSRT survey comprised pointed observations of preselected bright sources (>30 mJy) at $0.02 < z < 0.25$, typically reaching a 3σ optical depth sensitivity of 1% per channel width (16 km s^{-1}). They reported an overall detection rate of 27 ± 6%. MALS, as an untargeted survey, provides a representative sample down to much fainter flux densities (4 mJy) but at a lower overall sensitivity. To enable a comparison between these two surveys with different sensitivities, detection rates for a range of optical depth sensitivities are provided in the bottom half of Table 5 (see also Fig. 11). Our 3–5% detection rate for a high-τ population ($\int \tau dv > 5$ km s^{-1}) is consistent with the detection rate of Maccagni et al. (2017). This implies no significant redshift evolution in the properties of cold gas as probed by H I 21-cm absorption. Notably, when the two samples are matched in 1.4 GHz luminosity and $\int \tau_{3\sigma}\, dv$, the overall detection rates are $8.3^{+19.2}_{-6.9}$% (1/12) in MALS sample and $20.8^{+4.5}_{-3.8}$%(30/144) in Maccagni et al. (2017) sample, which are again consistent within the uncertainties.

Murthy et al. (2021) detected H I absorption in 19% of 26 radio loud AGNs at $0.25 < z < 0.4$ with the JVLA. Their sample was drawn exclusively from the bright, high-power end of the radio luminosity function (400–800 mJy; > 25.7 W Hz^{-1}). To ensure consistency with their reported sensitivities, we smoothed the MALS spectra to a velocity resolution of 50 km s^{-1}. Although the MALS and VLA samples have similar redshift distributions (KS test, p value = 0.12), they differ significantly in radio luminosity (p value = 4.2×10^{-19}). The VLA sample, as expected, is significantly more luminous (median log $L_{1.4\,GHz}$ (W Hz^{-1}) = 26.02) compared to the MALS sample (median log $L_{1.4\,GHz}$ (W Hz^{-1}) = 24.64). Nevertheless, the detection rates are consistent within uncertainties across all optical depth thresholds over the luminosity range log $L_{1.4\,GHz}$ (W Hz^{-1}) ~21.1–27.0. For instance, at $\int \tau_{3\sigma}\, dv < 5$ km s^{-1}, the detection rates are $6.4^{+6.2}_{-3.5}$% and $15.39^{+12.2}_{-7.4}$% for MALS and VLA samples, respectively. This further reinforces our finding that H I 21-cm detection rates show no significant dependence on either 1.4-GHz radio luminosity or redshift. Notably, Murthy et al. (2021) found no evidence of fast H I outflows (>1000 km s^{-1}). Our two blueshifted detections show moderate velocity offsets rather than extreme broad-wing outflow signatures. This uniform absence of fast atomic gas across both power regimes leaves open the fundamental question of why neutral outflow velocities do not scale with jet power. Future multifrequency data including high-resolution VLBI spectroscopy are needed to investigate how different factors including both intrinsic (such as jet energetics, the balance between kinetic and radiative feedback, the relative distribution of the gas with respect to the jet, source size, evolutionary stage, etc.) and extrinsic (e.g., sensitivity issues, orientation relative to the observer's line of sight) factors

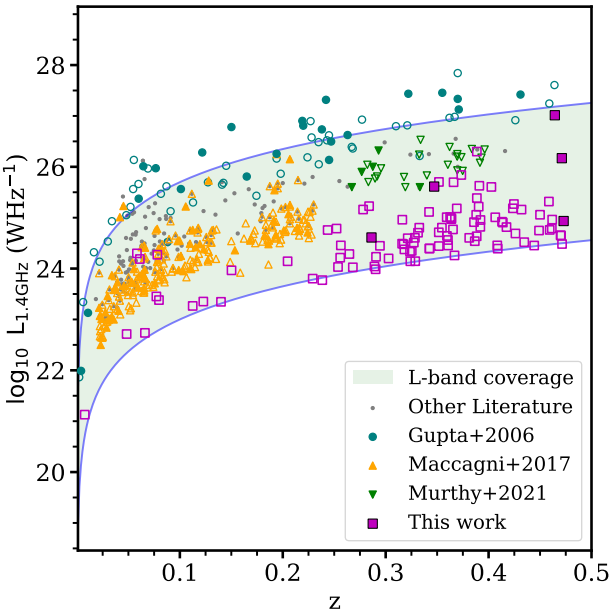


Fig. 11. $L_{1.4\,GHz}$ versus z at $z < 0.5$ for MALS HERGs and LERGs, Gupta et al. (2006), WSRT (Maccagni et al. 2017), and JVLA (Murthy et al. 2021) samples. Filled and open symbols represent H I detections and nondetections, respectively. Other literature sources shown for context include Glowacki et al. (2017); Chandola & Saikia (2017); Allison et al. (2012); Aditya & Kanekar (2018a,b); Chandola et al. (2020); Murthy et al. (2022). The shaded region denotes the MALS L-band search space, where the lower boundary corresponds to the 4 mJy flux density limit and the upper boundary represents a 2 Jy arbitrary flux density limit.

collectively govern the launch and detection of high-velocity neutral outflows (see Morganti 2017).

In comparison with the higher-redshift ($0.4 < z < 1.0$) First Large Absorption Survey in H I (FLASH; Allison et al. 2022; Aditya et al. 2024; Yoon et al. 2025), applying the exact observational cuts of Aditya et al. (2024) ($\int \tau_{3\sigma}\, dv < 9.08$ km s^{-1}) yields a MALS detection fraction of 3/56 ($5.4^{+5.2}_{-2.9}$%), which is consistent with their reported $1.8^{+4.0}_{-1.5}$%. However, this direct comparison is limited by sample disparities, as the current sample probes lower redshifts and lower radio luminosities with a strict focus on LERGs and HERGs, whereas Aditya et al. (2024) targets higher-luminosity AGNs in general.

4. Summary

We presented results from a search for cold neutral gas associated with radio-loud AGNs at $z < 0.5$, which spans ~36% of cosmic history, using H I 21-cm absorption line measurements from MALS. We crossmatched the MALS DR1 radio continuum catalog at 1006 MHz with the SDSS DR18 spectroscopic catalog to identify 1908 radio sources, of which 681 were classified as AGNs using BPT diagnostics and the Hα versus 1.4 GHz radio luminosity criterion. Optical emission-line fluxes were measured using the GELATOv2.5.2 software, and multiple line-ratio diagnostics combined with REWs of [O III]λ5007 were used to classify 426 of these AGNs into 327 LERGs and 99 HERGs. The LERGs showed significantly redder (>3σ) k-corrected $g-r$ optical colors, consistent with being hosted by older, more massive galaxies with suppressed star formation. The HERGs exhibited slightly steeper median radio spectral indices, reflecting a higher prevalence of FRII-type, lobe-dominated morphologies. When matched with the Best & Heckman (2012) catalog in 1.4 GHz luminosity bins, no statistically significant redshift dependence in the overall LERG fraction was found.

We searched for H I 21-cm absorption in a radio-bright subsample of 99 AGNs (79 LERGs, 20 HERGs) with peak flux densities $S_{1.4GHz} > 4$ mJy, and reported five new detections (four LERGs and one HERG). The sample spanning nearly six decades in radio luminosity ($\log L_{1.4\,GHz}$ (W Hz^{-1}) ~ 21.1–27.0), reaching luminosities an order of magnitude fainter than previous targeted H I absorption surveys. After accounting for varying optical depth sensitivities and the survey completeness, the overall detection rate was 3^{+3}_{-2}% at a 3σ integrated optical depth sensitivity threshold of 10.0 km s^{-1}. Comparison with the lower-redshift ($z < 0.25$) survey by Maccagni et al. (2017), matched in radio luminosity and integrated optical depth sensitivity, yielded consistent detection rates, suggesting little to no redshift evolution in the incidence of cold atomic gas out to $z \sim 0.5$. A comparison with the VLA survey of Murthy et al. (2021), which targeted significantly more luminous radio sources ($L_{1.4GHz} \sim 10^{25.7} - 10^{26.5}$ W Hz^{-1}) over a similar redshift range, yielded consistent detection rates across all optical depth thresholds, implying no significant dependence of the H I 21-cm detection rate on 1.4 GHz radio luminosity across $\log L_{1.4,GHz}$ (W Hz^{-1}) ~21.1–27.0.

The five absorbers exhibited complex and disturbed gas kinematics. In three systems the absorption was entirely redshifted relative to the systemic velocity, indicative of inflowing gas. In J0943–0004, the merger-driven origin of infalling gas is supported by the evidence of a nearby companion galaxy and double-peaked [O III]$\lambda\lambda$4959,5007 emission line. In J1455+0441, the absorption occurs asymmetrically against a lobe hotspot, potentially tracing gas from a faint companion galaxy at a projected distance of ~150 kpc from the core. In two systems, J0228−0107 and J1117−0235, the absorption is fully or predominantly blueshifted, indicating potential gas outflows that cannot be unambiguously attributed to specific jet-driven phenomena due to complex radio morphologies compounded by the limited availability of multifrequency VLBI data. H I profiles associated with LERGs display a wide range of asymmetries (A_p = 0.07–0.65) and velocity offsets exceeding 350 km s^{-1}, indicative of cold gas disturbed by jet–ISM interactions or lobe expansion, consistent with findings from lower-z samples (e.g. Glowacki et al. 2017; Chandola et al. 2020). The single HERG detection precludes a rigorous kinematic comparison between the two accretion modes. This limitation underscores the need for a substantially larger population of detections across both classes to statistically link H I kinematics with the underlying accretion states. Future work will extend this study to the full MALS AGN sample and to SF galaxies by combining MALS with upcoming spectroscopic releases from DESI (DESI Collaboration 2026) and 4MOST surveys (e.g., de Jong et al. 2019; Krogager et al. 2023).

Data availability

The full Table B.1 is available at the CDS via https://cdsarc.cds.unistra.fr/viz-bin/cat/J/A+A/713/A319.

Acknowledgements. We thank the anonymous referee for the insightful comments. The MeerKAT telescope is operated by the South African Radio Astronomy Observatory (SARAO; www.sarao.ac.za), which is a facility of the National Research Foundation, an agency of the Department of Science and Innovation. PPD hereby acknowledges the financial assistance of SARAO toward this research. The MeerKAT data were processed using the MALS computing facility at IUCAA (https://mals.iucaa.in/releases). The National Radio

Astronomy Observatory is a facility of the National Science Foundation operated under cooperative agreement by Associated Universities, Inc. This research has made use of NASA's Astrophysics Data System and the NASA/IPAC Extragalactic Database (NED), which is operated by the Jet Propulsion Laboratory, California Institute of Technology, under contract with the National Aeronautics and Space Administration.

References

Aditya, J. N. H. S., & Kanekar, N. 2018a, MNRAS, 473, 59
Aditya, J. N. H. S., & Kanekar, N. 2018b, MNRAS, 481, 1578
Aditya, J. N. H. S., Yoon, H., Allison, J. R., et al. 2024, MNRAS, 527, 8511
Allison, J. R., Curran, S. J., Emonts, B. H. C., et al. 2012, MNRAS, 423, 2601
Allison, J. R., Sadler, E. M., Amaral, A. D., et al. 2022, PASA, 39, e010
Baldwin, J. A., Phillips, M. M., & Terlevich, R. 1981, PASP, 93, 5
Barnes, J. E., & Hernquist, L. E. 1991, ApJ, 370, L65
Barnes, J. E., & Hernquist, L. 1996, ApJ, 471, 115
Best, P. N., & Heckman, T. M. 2012, MNRAS, 421, 1569
Best, P. N., Ker, L. M., Simpson, C., Rigby, E. E., & Sabater, J. 2014, MNRAS, 445, 955
Branch, M. A., Coleman, T. F., & Li, Y. 1999, SIAM J. Sci. Comput., 21, 1
Buttiglione, S., Capetti, A., Celotti, A., et al. 2010, A&A, 509, A6
Chambers, K. C., Magnier, E. A., Metcalfe, N., et al. 2016, arXiv e-prints [arXiv:1612.05560]
Chandola, Y., & Saikia, D. J. 2017, MNRAS, 465, 997
Chandola, Y., Saikia, D. J., & Li, D. 2020, MNRAS, 494, 5161
Chilingarian, I. V., Melchior, A.-L., & Zolotukhin, I. Y. 2010, MNRAS, 405, 1409
Cid Fernandes, R., Stasińska, G., Schlickmann, M. S., et al. 2010, MNRAS, 403, 1036
Combes, F., & Gupta, N. 2024, A&A, 683, A20
Cutri, R. M., Wright, E. L., Conrow, T., et al. 2021, VizieR Online Data Catalog: AllWISE Data Release (Cutri+ 2013), VizieR On-line Data Catalog: II/328. Originally published in: IPAC/Caltech
de Jong, R. S., Agertz, O., Berbel, A. A., et al. 2019, Messenger, 175, 3
Deka, P. P., Gupta, N., Chen, H. W., et al. 2024a, A&A, 687, A50
Deka, P. P., Gupta, N., Jagannathan, P., et al. 2024b, ApJS, 270, 33
DESI Collaboration (Abdul Karim, M., et al.) 2026, AJ, 171, 285
Duncan, K. J., Shivaei, I., Shapley, A. E., et al. 2020, MNRAS, 498, 3648
Dutta, R., Srianand, R., & Gupta, N. 2019, MNRAS, 489, 1099
Escott, E. L., Morabito, L. K., Scholtz, J., et al. 2025, MNRAS, 536, 1166
Fanaroff, B. L., & Riley, J. M. 1974, MNRAS, 167, 31
Gehrels, N. 1986, ApJ, 303, 336
Gitti, M., Brighenti, F., & McNamara, B. R. 2012, Adv. Astron., 2012, 950641
Glowacki, M., Allison, J. R., Sadler, E. M., et al. 2017, MNRAS, 467, 2766
Gupta, N., Salter, C. J., Saikia, D. J., Ghosh, T., & Jeyakumar, S. 2006, MNRAS, 373, 972
Gupta, N., Srianand, R., Baan, W., et al. 2018, in Proceedings of MeerKAT Science: On the Pathway to the SKA — PoS(MeerKAT2016), 277, 014
Gupta, N., Jagannathan, P., Srianand, R., et al. 2021, ApJ, 907, 11
Gupta, N., Shukla, G., Srianand, R., et al. 2022, ApJ, 929, 108
Gupta, N., Kerp, J., Balashev, S. A., et al. 2025, A&A, 698, A120
Hank, N. A. N., Verheijen, M. A. W., Blyth, S.-L., et al. 2025, MNRAS, 540, 3047
Hao, L., Strauss, M. A., Tremonti, C. A., et al. 2005, AJ, 129, 1783
Harrison, C. M., Alexander, D. M., Mullaney, J. R., & Swinbank, A. M. 2014, MNRAS, 441, 3306
Harrison, C. M., Costa, T., Tadhunter, C. N., et al. 2018, Nat. Astron., 2, 198
Heckman, T. M., & Best, P. N. 2014, ARA&A, 52, 589
Hopkins, A. M., Miller, C. J., Nichol, R. C., et al. 2003, ApJ, 599, 971
Hopkins, P. F., Hernquist, L., Cox, T. J., et al. 2006, ApJS, 163, 1
Hviding, R. E., Hainline, K. N., Rieke, M., et al. 2022, AJ, 163, 224
Ishibashi, W., Auger, M. W., Zhang, D., & Fabian, A. C. 2014, MNRAS, 443, 1339
Kewley, L. J., Groves, B., Kauffmann, G., & Heckman, T. 2006, MNRAS, 372, 961
Krogager, J. K., Gupta, N., Noterdaeme, P., et al. 2018, ApJS, 235, 10
Krogager, J. K., Leighly, K. M., Fynbo, J. P. U., et al. 2023, Messenger, 190, 38
Lu, Y., Wang, T., Zhou, H., & Wu, J. 2007, AJ, 133, 1615
Maccagni, F. M., Morganti, R., Oosterloo, T. A., Geréb, K., & Maddox, N. 2017, A&A, 604, A43
Morganti, R. 2017, Front. Astron. Space Sci., 4, 42
Mullaney, J. R., Alexander, D. M., Fine, S., et al. 2013, MNRAS, 433, 622
Murphy, E. J., Condon, J. J., Schinnerer, E., et al. 2011, ApJ, 737, 67
Murthy, S., Morganti, R., Oosterloo, T., & Maccagni, F. M. 2021, A&A, 654, A94
Murthy, S., Morganti, R., Kanekar, N., & Oosterloo, T. 2022, A&A, 659, A185
Perron-Cormier, M., Deg, N., Spekkens, K., et al. 2025, AJ, 169, 114
Planck Collaboration VI. 2020, A&A, 641, A6
Pracy, M. B., Ching, J. H. Y., Sadler, E. M., et al. 2016, MNRAS, 460, 2
Shen, Y., Richards, G. T., Strauss, M. A., et al. 2011, ApJS, 194, 45
Singha, M., O'Dea, C., Gordon, Y., Lawlor-Forsyth, C., & Baum, S. 2021, in American Astronomical Society Meeting Abstracts, 53, 209.07
Tadhunter, C. N., Morganti, R., Robinson, A., et al. 1998, MNRAS, 298, 1035
Team, T. C., Bean, B., Bhatnagar, S., et al. 2022, PASP, 134, 114501
van Gorkom, J. H., Knapp, G. R., Ekers, R. D., et al. 1989, AJ, 97, 708
Vazdekis, A., Koleva, M., Ricciardelli, E., Röck, B., & Falcón-Barroso, J. 2016, MNRAS, 463, 3409
Wright, E. L., Eisenhardt, P. R. M., Mainzer, A. K., et al. 2010, AJ, 140, 1868
Yoon, H., Sadler, E. M., Mahony, E. K., et al. 2025, PASA, 42, e088

Appendix A: Representative optical spectra and Diagnostic framework

In this section, we present representative fits to the optical spectra performed with GELATO and describe the diagnostic framework used to classify AGNs.

An AGN may be classified as LERG or HERG based on the set of five diagnostics listed in Section 2.5. For each diagnostic, we define a confidence measure C depending on following three factors, f_i, with $|f_i| \in [0, 1]$:

1. Line Quantity Factor (f_1): This reflects the number of emission lines used in the classification,
$$f_1 = \frac{N_{\rm lines} - N_{\rm min}}{N_{\rm max} - N_{\rm min}},$$
where $N_{\rm max} = 6$ and $N_{\rm min} = 1$.

2. S/N Factor (f_2): This accounts for the minimum S/N used among the lines,
$$f_2 = \frac{1}{1 + \exp[-k_1(\mathrm{S/N_{min}} - \mathrm{S/N_0})]},$$
with $\mathrm{S/N_0} = 3$ as a reference threshold and we assume $k_1 = 2$, that controls the steepness of the function.

3. Distance from Boundary (f_3): This measures distance of the source in the units of uncertainty from the diagnostic-specific segregation boundary,
$$f_3 = \frac{1}{1 + \exp[-k_2(\Delta - 1)]},$$
where $\Delta = |x - x_{\rm div}|/\sigma$ and steepness parameter $k_2 = 2$.

The confidence measure, C, for a diagnostic is the weighted average of f_i's with weights w_i as $\mathrm{C} = \sum w_i f_i$, where $i = 1, 2$ and 3. We assume equal weights, $w_1 = w_2 = w_3 = \frac{1}{3}$, to assign equal importance to all three factors. We assign a negative sign for LERGs and a positive sign for HERGs. Each diagnostic is also assigned a reliability factor $R \in [0, 1]$. The final significance (S) for the classification of a source is then calculated as,

$$S = \frac{\sum_{i=1}^{5} R_i \cdot C_i}{\sum_{i=1}^{5} R_i}, \tag{A.1}$$

The EI-based diagnostic (Diagnostic 1) is inapplicable to AGNs with broad Balmer components (Buttiglione et al. 2010). Therefore, to identify optimal weights, we used 433 narrow-line AGNs (Table 1). A sequential application of these diagnostics identifies: 11 HERGs and 21 LERGs (Diagnostic 1), 10 HERGs and 22 LERGs (Diagnostic 2), 27 HERGs and 107 LERGs (Diagnostic 3), 10 HERGs and 8 LERGs (Diagnostic 4), and 13 HERGs and 147 LERGs (Diagnostic 5). Clearly, more objects are classified as subsequent less stringent diagnostics are used. In total, 376 out of 531 AGNs get classified using at least one diagnostic method in to 70 HERGs and 306 LERGs.

In comparison to the above, adopting uniform weights ($R_i = 1$), implying no preference for any diagnostic, we get 60 HERGs and 236 LERGs. However, to better align with sequential classification used in the literature, we adopted $R_1 = 1, R_2 = R_3 = 0.9$, $R_4 = 0.8$ and $R_5 = 0.5$. The distribution of significances are shown in Fig. A.1. This yields 68 HERGs and 308 LERGs, with a few notable exceptions highlighting the objectivity of our approach. For example, J091103.75+191752.0 – was initially classified as a HERG based solely on [O III] REW of 9.5 ± 0.8 Å,

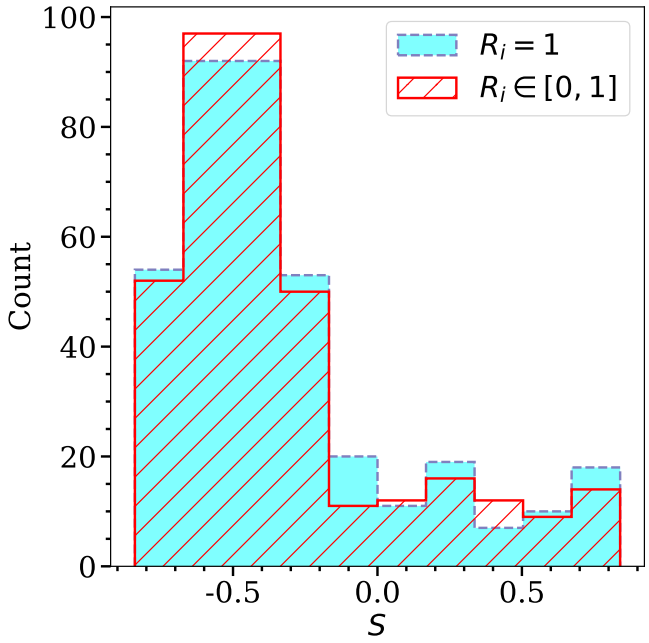


Fig. A.1. Distribution of significance scores (S) for LERG and HERG classification. The cyan-filled histogram represents equal weights ($R_i = 1$), while the red-hatched histogram shows the distribution using the diagnostic-specific weights – $R_1 = 1, R_2 = R_3 = 0.9, R_4 = 0.8$, and $R_5 = 0.5$.

but our final significance score ($S \sim -0.21$) correctly identifies it as a LERG (see also last paragraph of Section 2.5).

It is particularly intriguing to test the classifications of 160 AGNs initially categorized using only weak-line diagnostics of Cid Fernandes et al. (2010) (Diagnostic 5). To facilitate this, we lowered the line flux S/N threshold to 1 to incorporate additional diagnostics where possible. For 10 sources – J101133.55+155812.9 ($S \sim -0.20$), J012858.28+141337.7 ($S \sim -0.25$), J001450.80+082545.0 ($S \sim -0.20$), J002205.85+060317.1 ($S \sim -0.14$), J010531.54+045309.9 ($S \sim -0.23$), J130746.13+080108.1 ($S \sim -0.17$), J083821.14+034405.7 ($S \sim -0.19$), J230225.22+055418.2 ($S \sim -0.39$), J092728.26+020438.6 ($S \sim -0.37$), and J225804.30−102143.7 ($S \sim -0.43$) – the resulting significance scores indicated a different classification than before.

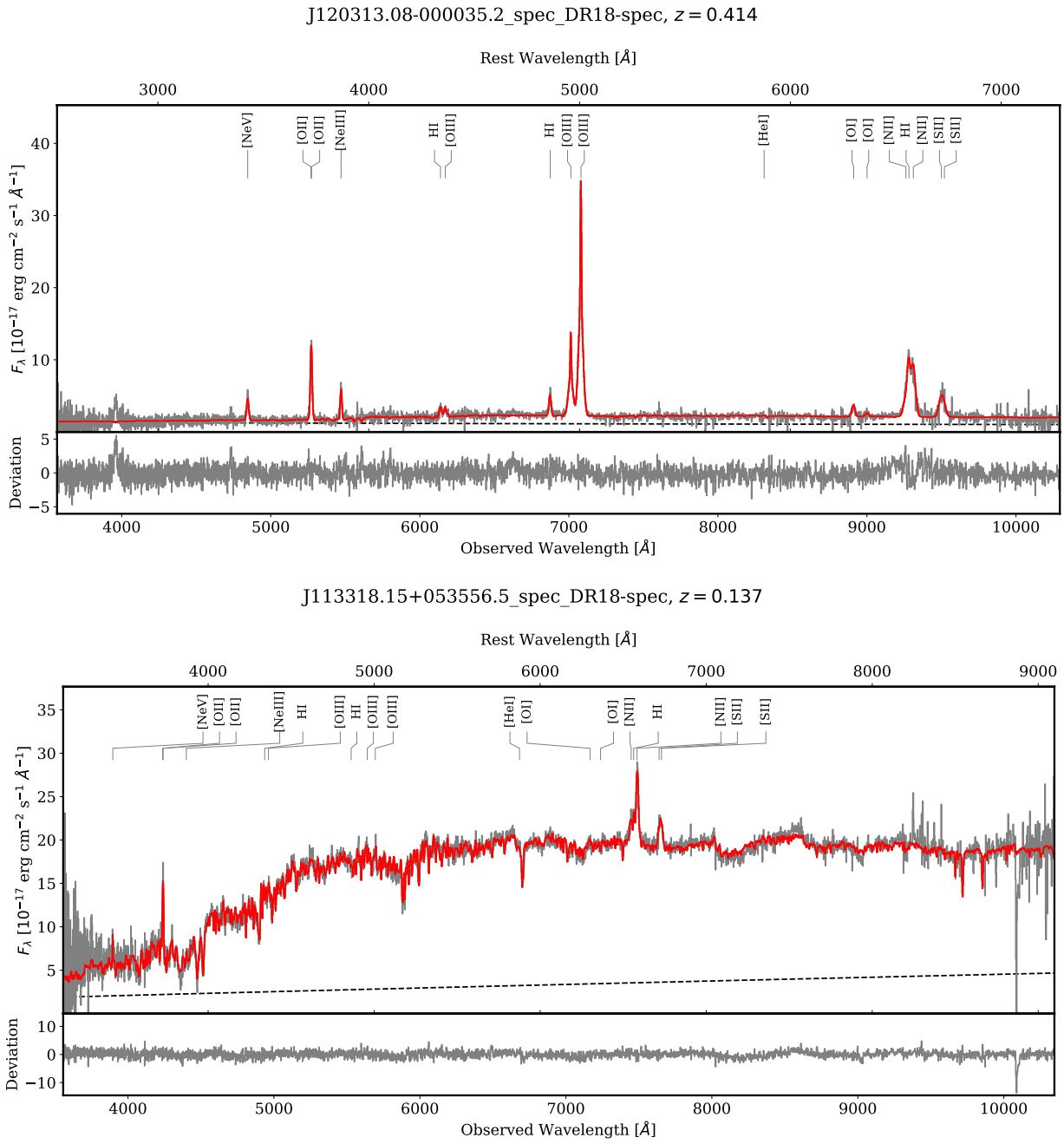


Fig. A.2. Representative spectra classified via the EI (`Diagnostic 1`), showing a HERG (Top) and LERG (bottom). In each panel, the upper sub-panel shows the SDSS spectrum (gray), the `GELATO` fit (red), and the positions of emission-line components (Table 1). The lower sub-panel shows the residuals, normalized by error.

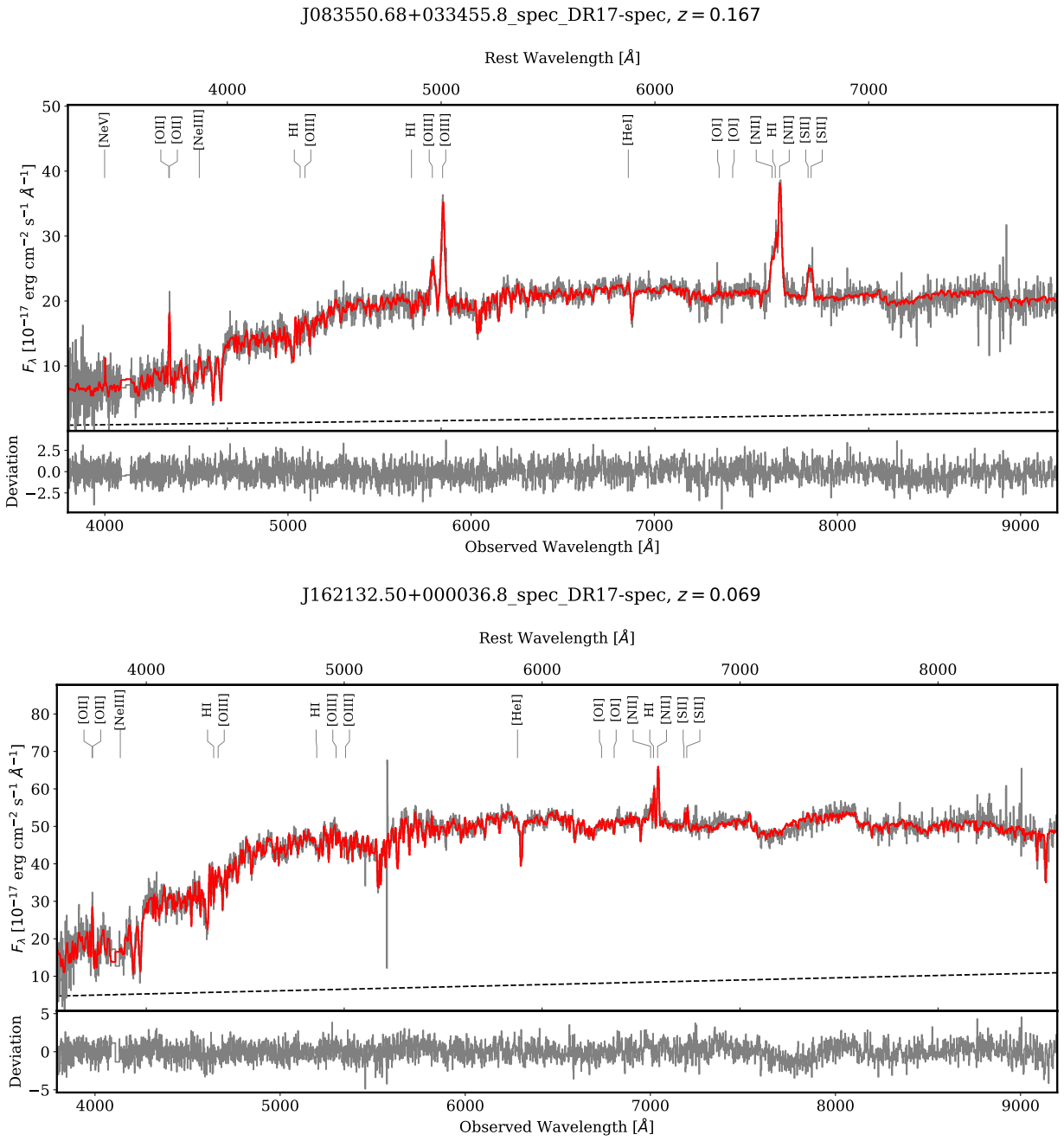


Fig. A.3. Representative spectra classified using the diagnostic diagrams from Kewley et al. (2006) (`Diagnostic 2`). J083550.68+033455.8 is a HERG (top), while J162132.50+000036.8 is a LERG (bottom) – both classified using the [O III]/Hβ versus [S II]/Hα diagnostic given in the text.

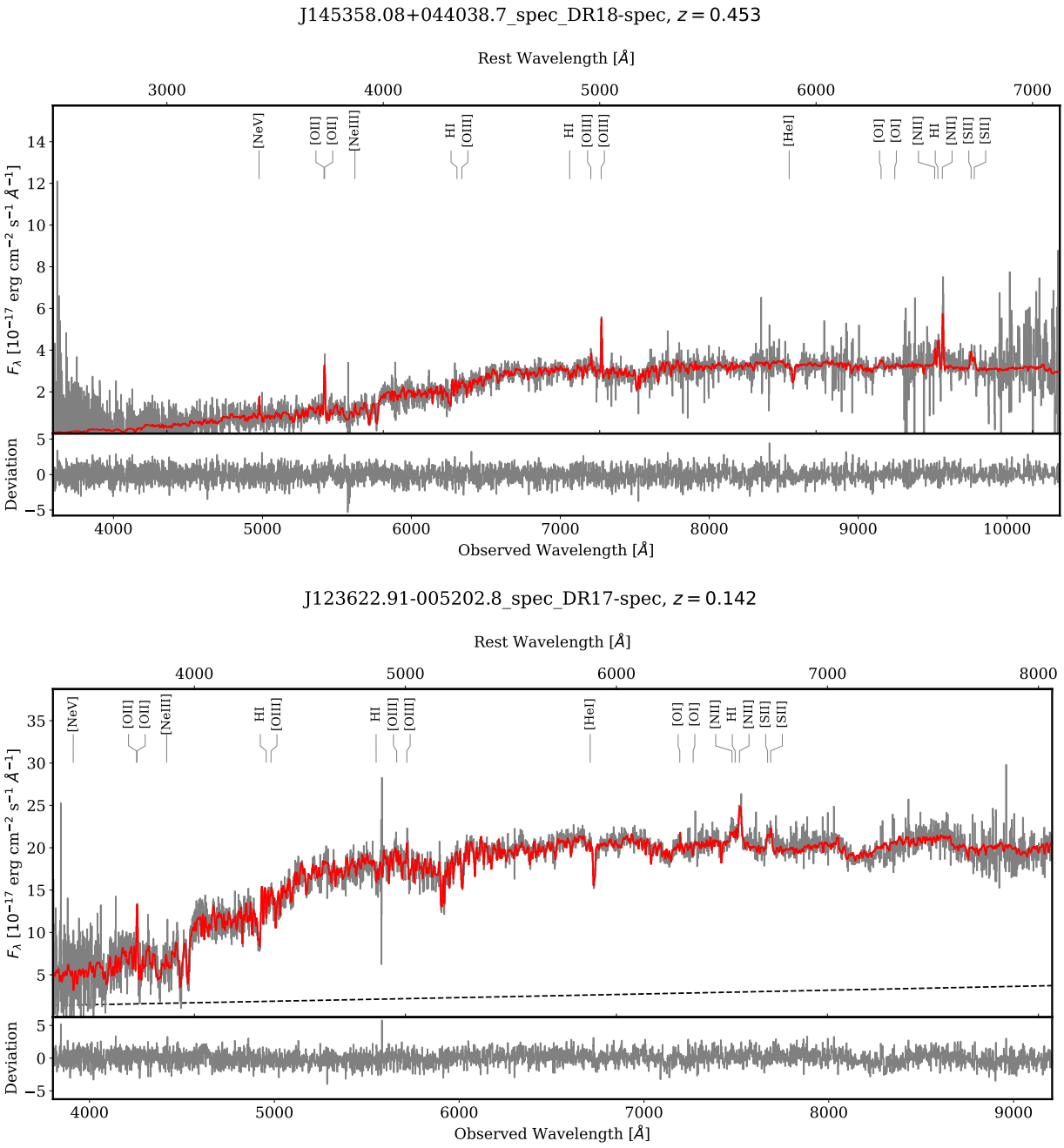


Fig. A.4. Representative spectra of a HERG (top) and a LERG (bottom), classified based on the [O III] λ5007 rest-frame equivalent width (`Diagnostic 3`).

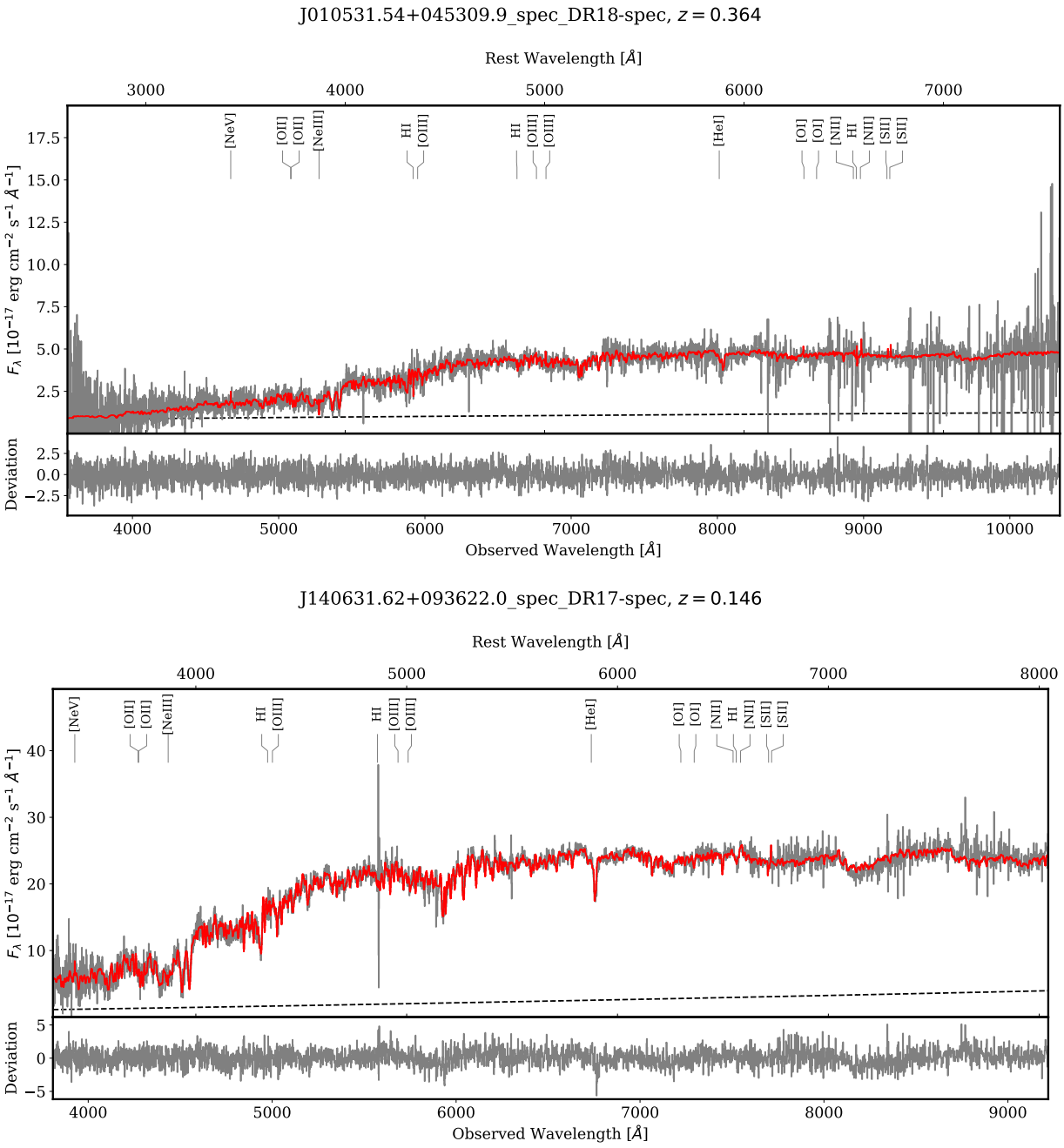


Fig. A.5. Representative spectra classified using the diagnostic diagram from Cid Fernandes et al. (2010) (`Diagnostic 5`). A HERG spectrum (top), while a LERG spectrum (bottom) – both classified using the [O III]/Hα versus [N II]/Hα diagnostic given in the text.

Appendix B: MALS-SDSS sample

Table B.1 presents the first 10 rows of the MALS-SDSS sample of 1300 sources. Of these, 426 are classified into LERGs (327) and HERGs (99), with the full list available at the CDS.

Table B.1. MALS-SDSS sample classified into SF galaxies, composite galaxies, and AGNs (LERGs and HERGs).

Source	MALS RA (deg)	MALS DEC (deg)	z	$S_{1.4GHz}$ (mJy)	$\log L_{1.4GHz}$ (W Hz^{-1})	Class	S	Spectroscopic Class
(1)	(2)	(3)	(4)	(5)	(6)	(7)	(8)	(9)
J000002.61+200307.3	0.01091	20.05205	0.279	0.7	23.33	COMP	–	–
J000334.74−050307.4	0.89476	−5.05208	0.499	1.8	24.22	AGN	–	–
J000337.42−053401.6	0.90595	−5.56711	0.396	3.1	24.21	AGN	–	–
J000432.52−045650.9	1.13554	−4.94748	0.243	13.7	24.37	AGN	–	–
J000449.86+174303.4	1.20777	17.71763	0.446	1.7	24.07	AGN	−0.17	LERG
J000519.61−050810.3	1.33174	−5.13622	0.241	3.1	23.71	AGN	–	–
J000747.87+165900.9	1.94949	16.98359	0.403	6.3	24.57	AGN	–	–
J000756.44+175635.5	1.98517	17.94320	0.453	3.8	24.44	AGN	0.84	HERG
J001218.32+084415.2	3.07634	8.73757	0.261	1.5	23.29	AGN	–	–
J001237.48+084353.7	3.15620	8.73159	0.165	22.4	24.23	AGN	–	–

Notes. Column 1: MALS-SPW2 source ID. Column 2 – 3: MALS right ascension and declination, both in degrees. Column 4: SDSS spectroscopic redshift. Column 5: flux density at 1.4 GHz in mJy. Column 6: log radio luminosity at 1.4 GHz. Column 7: classification into AGN, SF, and composite (COMP) systems, Column 8: Significance score as defined in equation A.1. Column 9: Optical spectroscopic classification.

Appendix C: Optical images of AGN with 21-cm absorption detections

Fig. C.1 shows optical color composite (g, r, i) images from Pan-STARRS1 for the five sources displaying associated H I 21-cm absorption (Table 4).

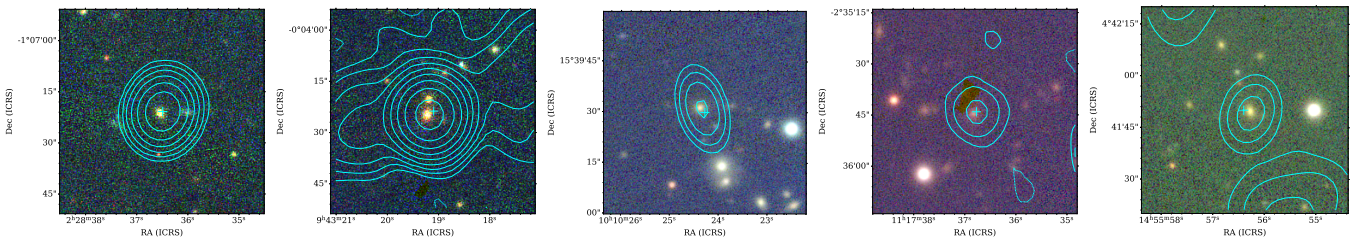


Fig. C.1. From left to right: J022836.49-010720.8, J094319.09-000423.7, J101024.28+153929.9, J111736.77-023544.0, and J145556.40+044150.0. The radio contours match the cyan contours shown in Fig. 8, while the '+' marks the mean radio source position.